

# Recent Progress in Low Threshold Plasmonic Nanolasers

Ru Wang, Chunfeng Wang,\* Yi Ma, Jianli Sun, Peiguang Yan, Chunxiang Xu,\*  
and Caofeng Pan\*

Plasmonic nanolasers as a new class of coherent laser beyond the diffraction limit have attracted a lot of attention. However, the ultrahigh optical confinement caused by the plasmon effect is inevitably accompanied by metal absorption loss, thus increasing the pump threshold of the plasmonic nanolaser. In the past decade, many good results about low threshold plasmonic nanolasers have been realized and successfully extended to various applications. Here, this advance is discussed and some opinions are offered. First, based on the theoretical model and key parameters of the plasmonic nanolaser, the factors affecting the threshold are analyzed. Subsequently, the experimental efforts on the realization of low threshold plasmonic nanolasers from optical pumping to electrical pumping are reviewed. Their applications in on-chip optical interconnects, biochemical analysis, and far-field structure are then considered. Finally, feasible approaches to threshold reduction are discussed, as well as more possible applications in the future.

various human activities from scientific research to daily life.<sup>[1–4]</sup> The rapid developments of microlasers such as vertical cavity surface emitting lasers,<sup>[5,6]</sup> microdisk lasers,<sup>[7,8]</sup> and photonic crystal lasers<sup>[9,10]</sup> over the past few decades have opened up entirely new opportunities for on-chip optical interconnections,<sup>[11–13]</sup> super-resolution nanolithography<sup>[14–16]</sup> and nanospectroscopy.<sup>[17–20]</sup> However, because of the limited effective refractive index, the size of traditional dielectric cavities is essentially limited by the optical diffraction limit, which hinders the process of miniaturization.<sup>[21–24]</sup> Surface plasmons (SPs) are collective oscillation of quasi-free electrons between the interface of dielectric and metal, which are characterized by ultra-high optical confinement and ultra-fast relaxation processes.<sup>[25–27]</sup> The introduction of metal with negative dielectric

## 1. Introduction

Laser is a light source with high directionality and coherence. Since its invention in 1960, laser has played an important role in

permittivity is one of the most feasible ways to compress the cavity.<sup>[28]</sup> Using mode size of a plasmonic cavity with far below the diffraction limit, extremely small cavity sizes realize in one or more dimensions, resulting in laser generation under extreme conditions. This is the plasmonic nanolaser (Surface plasmon amplification by stimulated emission, Spaser), a concept proposed by Bergman and Stockman in 2003.<sup>[29]</sup> Its operation mechanism is similar to that of a traditional laser. Subsequently, in 2009, three groups experimentally demonstrated the feasibility of plasmonic nanolasers from three confinement dimensions, and their superior performance have attracted strong attention from industrial world and academic world.<sup>[30–33]</sup>

The ultrahigh optical confinement of electromagnetic field in plasmonic nanolaser caused by the SPs leads to high Purcell factor, which is inevitably accompanied by ultra-high energy loss. On the one hand, high Purcell effect imply high the spontaneous emission coupling factor  $\beta$ , resulting in reduction of the threshold. On the other hand, high Purcell factor enhance energy dissipation, and faster decay rate inhibits population inversion, resulting in the increase of threshold. Therefore, it is very important to clarify the factors that affect the threshold of plasmonic nanolaser. In recent years, as shown in **Figure 1**, low-threshold plasmonic nanolasers at different wavelengths were realized by using single-crystal metal microsheets (Al, Ag, Au), single-crystal thin films (Na) and high-gain materials (ZnO, GaN, CdS, Perovskite, etc.). In addition, great progress has been made in reducing the threshold of plasmonic nanolasers with the application of low operating temperature, optimization of structure design of the optical confinement, improvement of laser

R. Wang, P. Yan, C. Pan  
College of Physics and Optoelectronic Engineering  
Shenzhen University  
Shenzhen 518060, P. R. China  
E-mail: cfpan@binn.cas.cn

R. Wang, C. Pan  
CAS Center for Excellence in Nanoscience  
Beijing Key Laboratory of Micro-nano Energy and Sensor  
Beijing Institute of Nanoenergy and Nanosystems  
Chinese Academy of Sciences  
Beijing 101400, P. R. China

C. Wang  
College of Materials Science and Engineering  
Guangdong Research Center for Interfacial Engineering of Functional  
Materials  
Shenzhen University  
Shenzhen 518060, P. R. China  
E-mail: cfwang@szu.edu.cn

Y. Ma, J. Sun, C. Xu  
State Key Laboratory of Bioelectronics  
School of Biological Sciences & Medical Engineering  
Southeast University  
Nanjing 210096, P. R. China  
E-mail: xcxseu@seu.edu.cn

 The ORCID identification number(s) for the author(s) of this article can be found under <https://doi.org/10.1002/adom.202203137>

DOI: 10.1002/adom.202203137

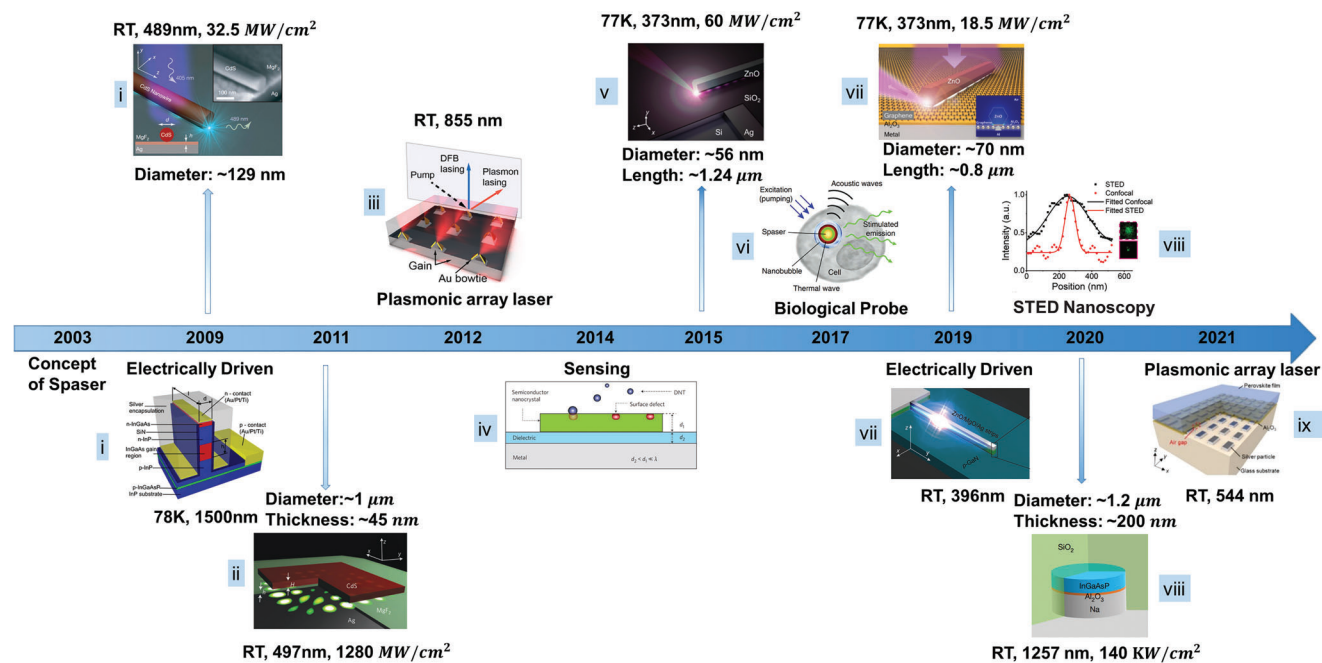


**Figure 1.** Development of plasmonic nanolasers, including: device size, threshold evolution, laser wavelength, operating temperature, and application aspects. i) Upper: Reproduced with permission.<sup>[31]</sup> Copyright 2009, NPG. Lower: Reproduced with permission.<sup>[32]</sup> Copyright 2009, OSC. ii) Lower: Reproduced with permission.<sup>[140]</sup> Copyright 2011, NPG. iii) Upper: Reproduced with permission.<sup>[50]</sup> Copyright 2012, ACS. iv) Lower: Reproduced with permission.<sup>[40]</sup> Copyright 2014, NPG. v) Upper: Reproduced with permission.<sup>[136]</sup> Copyright 2015, ACS. vi) Upper: Reproduced with permission.<sup>[45]</sup> Copyright 2017, NPG. vii) Upper: Reproduced with permission.<sup>[139]</sup> Copyright 2019, ACS. Lower: Reproduced with permission.<sup>[159]</sup> Copyright 2019, Wiley-VCH. viii) Upper: Reproduced with permission.<sup>[46]</sup> Copyright 2020, Wiley-VCH. Lower: Reproduced with permission.<sup>[151]</sup> Copyright 2020, NPG. ix) Lower: Reproduced with permission.<sup>[64]</sup> Copyright 2021, Wiley-VCH.

preparation technology and synthesis method. And many of these low threshold plasmonic nanolasers have been used in various fields including on-chip optical interconnections,<sup>[34–39]</sup> biochemical analysis,<sup>[40–47]</sup> and far-field applications.<sup>[41,48–65]</sup> Obviously, in the whole development of plasmonic nanolasers, reducing the threshold is always an inescapable topic, and some new achievements and applications have emerged in recent years. Therefore, it is necessary to revisit the threshold about plasmonic nanolaser.

In this paper, we review the recent advance of plasmonic nanolaser about both the aspect of low-threshold devices and applications. First, based on theoretical model and key parameters of plasmonic nanolaser, the factors affecting the threshold are analyzed. Subsequently, we review the experimental efforts on realization of low threshold plasmonic nanolasers from optical pumped to electric pumped and their applications in on-chip optical interconnects, biochemical analysis and far-field structure. Finally, we discuss feasible approaches to threshold reduction, as well as more possible applications in the future.

## 2. The Concept of Surface Plasmons

SPs are collective response of free electrons on a metal surface, which include two important forms of localized surface plasmons (LSPs) and propagating surface plasmon (PSPs).<sup>[78]</sup> The resonance response of free electrons can be realized by coupling with the incident light.<sup>[66]</sup> Due to their strong local space characteristics and field enhancement characteristics, SPs have been widely

applied in widely used in spectroscopy,<sup>[67,68]</sup> optoelectronics,<sup>[69–71]</sup> imaging,<sup>[72,73]</sup> biosensing,<sup>[74,75]</sup> as well as nanophotonics.<sup>[76,77]</sup>

### 2.1. Localized Surface Plasmons

LSPs are collective resonance of localized electrons caused by metal nanoparticles (NPs), as shown in **Figure 2a**.<sup>[79]</sup> When the frequency of the incident light matches the resonance that of the metal NPs, LSPs on the metal NPs are excited.<sup>[80,81]</sup> The frequency of their resonance were related to the shape and size of the metal NPs and the dielectric constant of the surrounding environment. The polarizability of the spherical metal NPs can be calculated by following Equation (1):

$$P = 4\pi a^3 \frac{\epsilon_d - \epsilon_m}{\epsilon_d + 2\epsilon_m} \quad (1)$$

Here,  $a$  is the diameter of NPs,  $\epsilon_d$  and  $\epsilon_m$  is permittivity of surrounding dielectric and metal NPs respectively. According to Equation (1), When  $\epsilon_m = -2\epsilon_d$ ,  $P$  reaches its maximum value, resulting in resonance. Due to the stimulated plasmon cannot propagate in the nanostructure, this process is called localized surface plasmons resonance (LSPR). The local enhancement of the electromagnetic field on metal NPs can lead to effective light concentration with the enhancement factor up to 100.<sup>[82–87]</sup> The electromagnetic field near the metal NPs decays exponentially along the metal NPs surface.<sup>[25]</sup> The attenuation length of the electric field is usually related to the order of magnitude of the

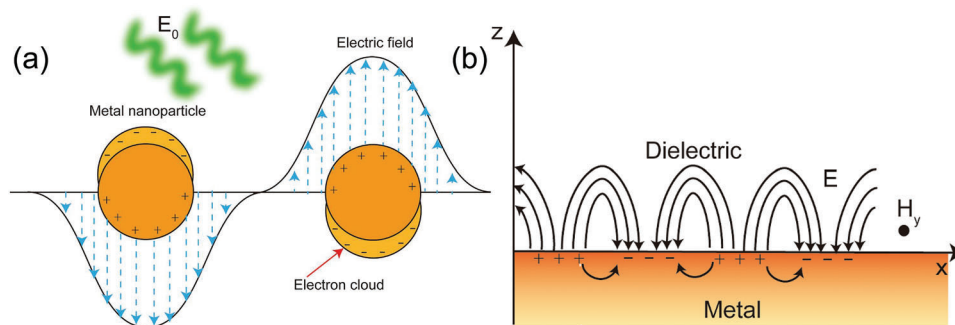


**Figure 2.** a) Schematic diagram of LSPs on spherical metal nanoparticles;<sup>[160]</sup> b) Schematic diagram of the PSPs mode at the interface of metal and dielectric materials.<sup>[166]</sup>

particle size, but also depends on the surrounding environment and the dielectric properties of the metal material itself, which provides flexibility for selecting materials whose gain spectrum overlaps with the resonant frequency.<sup>[88–102]</sup> Equation (1) is used only for very small metal NPs, while the polarization of large metal particles is governed by Mie theory. Plasmonic nanolasers can be constructed on the basis of these metal NPs using local surface plasmons. By replacing the surrounding dielectric layer with gain medium, the particle itself can act as a resonator.

## 2.2. Propagating Surface Plasmons

The dielectric function of metal is dispersive and can be calculated as following formula,

$$\epsilon_m(\omega) = \epsilon'_m(\omega) + i\epsilon''_m(\omega) \quad (2)$$

Different from the dielectric function of metal, that of medium is a positive real function. In classical electromagnetic images, SPs is the surface mode solution of Maxwell's equations under interface boundary conditions. In the case of planar interfaces, transverse magnetic (TM) waves polarized relative to the incident plane can excite the SPs mode at the metal-dielectric interface. As shown in Figure 2b, PSPs exist at interface of metal-dielectric (simplest SP waveguide).<sup>[66,103]</sup> Using the surface mode solution, the electric field of PSPs along the x-direction propagation can be expressed as follows.

$$E(x) = E_0 \exp [i(k'_{SP} + ik''_{SP}) \cdot x - i\omega t] \quad (3)$$

$$I(x) = E^2 = I_0 \exp(-2k''_{SP}x) \equiv I_0 \exp\left(-\frac{x}{L_{SP}}\right) \quad (4)$$

$$\lambda_{SP} = \frac{2\pi}{k'_{SP}} \quad L_{SP} = \frac{1}{2k''_{SP}} \equiv \frac{1}{\alpha_{SP}} \quad (5)$$

$I(x)$  is the electric field intensity of SPs mode,  $\lambda_{SP}$  is wavelength of SPs mode,  $L_{SP}$  is the propagation length (the 1/e decay length along x-direction propagation),  $\alpha_{SP}$  is absorption coefficient of SPs. The dispersion relation of SPs mode is as follows:

$$k_{SP} = k'_{SP} + ik''_{SP} = k_0 \sqrt{\frac{\epsilon'_m \epsilon_d}{\epsilon'_m + \epsilon_d}} \quad (6)$$

The real part of  $k_{SP}$  determines the wavelength of SPs, while the imaginary part of that determines the damping of SPs. The SPs mode propagates along the x-direction at the metal-dielectric interface. In order to get a propagating SPs,  $k'_{SP}$  and  $k''_{SP}$  need to be real. Therefore,  $k'_{SP}$  and  $k''_{SP}$  can obtain:

$$k'_{SP} \approx k_0 \sqrt{\frac{\epsilon'_m \epsilon_d}{\epsilon'_m + \epsilon_d}}, \quad k''_{SP} \approx k_0 \left( \frac{\epsilon'_m \epsilon_d}{\epsilon'_m + \epsilon_d} \right)^{3/2} \frac{\epsilon''_m}{2(\epsilon'_m)^2} \quad (7)$$

And the requirements of  $k'_{SP}$  include the following conditions:

$$\epsilon'_m(\omega) + \epsilon_d(\omega) < 0 \quad (8)$$

For noble metal, such as Ag and Au, this condition is usually satisfied in the visible and near infrared waveband. Thus, SPs mode exists at the Ag/dielectric (Au/dielectric) interface, as well as at the Ag/Silicon (Au/Silicon) interface. The real part of permittivity of noble metals is much larger than the imaginary part, this is  $\epsilon''_m \ll |\epsilon'_m|$ . Then  $L_{SP}$  can be transformed into

$$L_{SP} = \frac{1}{2k''_{SP}} \approx \frac{1}{k_0} \left( \frac{\epsilon'_m + \epsilon_d}{\epsilon'_m \epsilon_d} \right)^{3/2} \frac{(\epsilon'_m)^2}{\epsilon''_m} \quad (9)$$

From the formula, for purpose of obtaining a long propagation length, it is necessary to using a metal dielectric function with the larger  $\epsilon'_m$  and the smaller  $\epsilon''_m$ . In addition, the introduction of gain medium is considered to compensate loss for allowing the SPs to propagate longer distances in the plasmonic structure. The small-signal gain of dyes, semiconductors is 1000–2000  $\text{cm}^{-1}$  for interface of planar metal-dielectric, 2000–5000  $\text{cm}^{-1}$  along the thin metal coated waveguide ( $\approx 50$  nm), 3000  $\text{cm}^{-1}$  for resonant LSPs of metal NPs, 80 000  $\text{cm}^{-1}$  for SPs to approach their energy asymptote.<sup>[104]</sup> Therefore, SPs amplification and plasmonic nanolasers have attracted great attention and make remarkable progress in the last few years.

## 3. The Fundamental Theory of Plasmonic Nanolaser

### 3.1. The Concept of Plasmonic Nanolaser

Surface plasmon amplification by stimulated emission of radiation (Spaser),<sup>[105,106]</sup> an emerging nano-coherent light source,

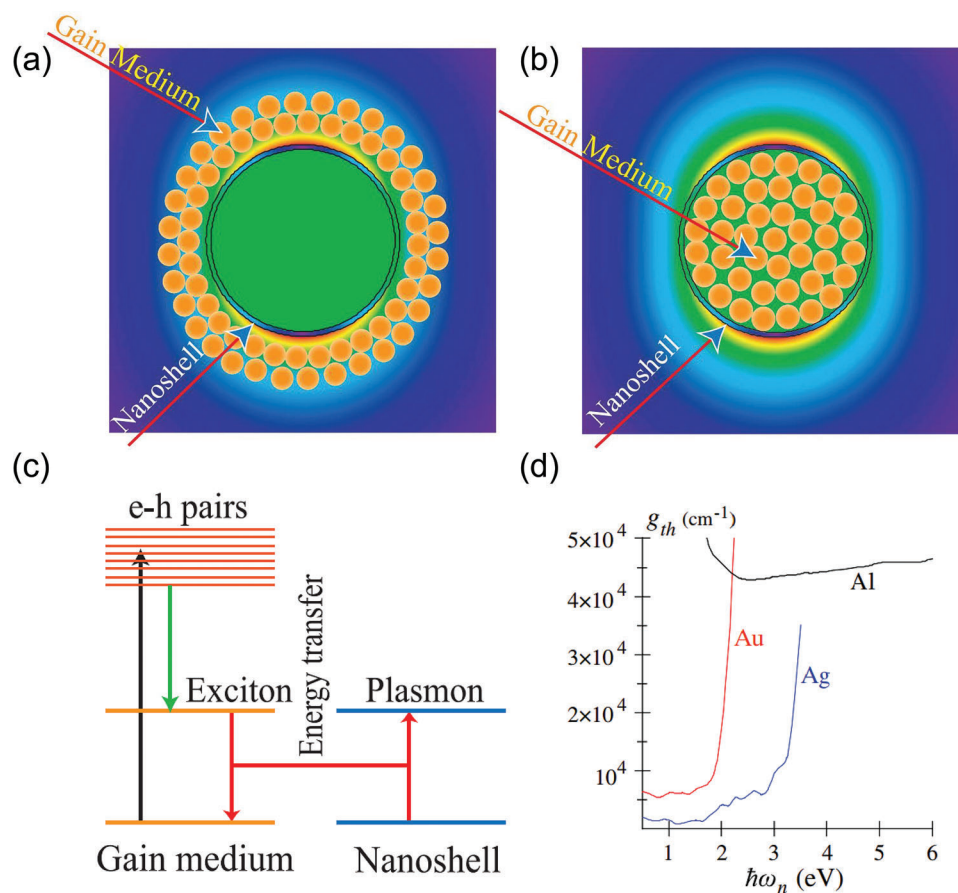


**Figure 3.** Schematic of spaser.<sup>[106]</sup> a) The gain medium outside of the shell with metal nanoshell resonance mode (Dipole mode); b) The same as (left) but for the gain medium inside the shell with metal nanoshell resonance mode (quadrupole mode); c) Schematic diagram of spasing process proposed by Bergman and Stockman;<sup>[106]</sup> (a–c) Reproduced with permission.<sup>[106]</sup> Copyright 2010, IOP Publishing. d) Threshold gain required by spaser behavior.<sup>[107]</sup> Reproduced with permission.<sup>[107]</sup> Copyright 2011, APS.

was first proposed by Bergman and Stockman in 2003.<sup>[29]</sup> Generally, plasmonic nanolaser include three parts: gain material, plasmonic cavity, and pumping source (Figure 3a). Figure 3b is a schematic diagram of the spasing process. The specific process is: an excitation turns the transition into an electron-hole pair, which relaxes to the exciton energy level. The energy generated by the exciton recombination is transferred to the plasmon excitation of the metal through resonant coupling. The plasmon excitation excites this emission, giving a feedback to Spaser behavior.

Among them, active material is a three-level gain medium, such as dye molecules and semiconductor, etc. A realistic gain of  $g \sim 10^4 \text{ cm}^{-1}$  can be obtained for dye molecules or direct bandgap semiconductors. In terms of plasmonic cavity, different metals can be selected according to the different luminance bands, as shown in Figure 3c. The threshold gain of plasmonic cavity materials is calculated in the near-infrared, visible and ultraviolet regions.<sup>[107]</sup> In their study, considering the large coherent SPs per mode interval and the relatively low threshold gain, Ag and Au can be chosen in the visible waveband ( $<10\,000 \text{ cm}^{-1}$ ), while Al is a better choice in the ultraviolet waveband ( $<50\,000 \text{ cm}^{-1}$ ).<sup>[107]</sup> In addition to this, recent studies have shown that metal Na has a better SPs response in the infrared spectral region.<sup>[151]</sup>

### 3.2. Mode Characteristics in Plasmonic Nanocavity

The plasmonic nanocavity shown in Figure 4a consists of ZnO semiconductor nanowire (cylinder waveguide) embedded in  $\text{SiO}_2$  near a Ag surface (SPs waveguide). We use it as an example to illustrate mode characteristics (effective refractive index, modal area, propagation distance, waveguide confinement factor, and transparency gain) in hybrid plasmonic nanocavity.

The hybrid mode (the lower index hybrid mode cannot exist) is expressed by coupled-mode theory in ZnO/insulator/Ag structure (SIM):<sup>[111]</sup>

$$\psi(r, h) = a(r, h) \psi_{\text{cyl}}(r) + b(r, h) \psi_{\text{SP}} \quad (10)$$

$a(r, h)$  and  $b(r, h)$  are the amplitudes of SP waveguide and cylinder waveguide, respectively. The hybrid modes can be characterized by an effective refractive index  $n_{\text{hyb}}(r, h)$  that is proportional to the real part of their eigenvalues, quantifying the phase velocity in the propagation direction. For better understanding, we will analyze the dependence of the effective index  $n_{\text{hyb}}(r, h)$  of the hybrid mode on  $r$  and  $h$ . As shown in Figure 4b, effective index of hybrid waveguide mode is always larger than that of cylinder waveguide mode. It predicts the different between cylindrical and hybrid

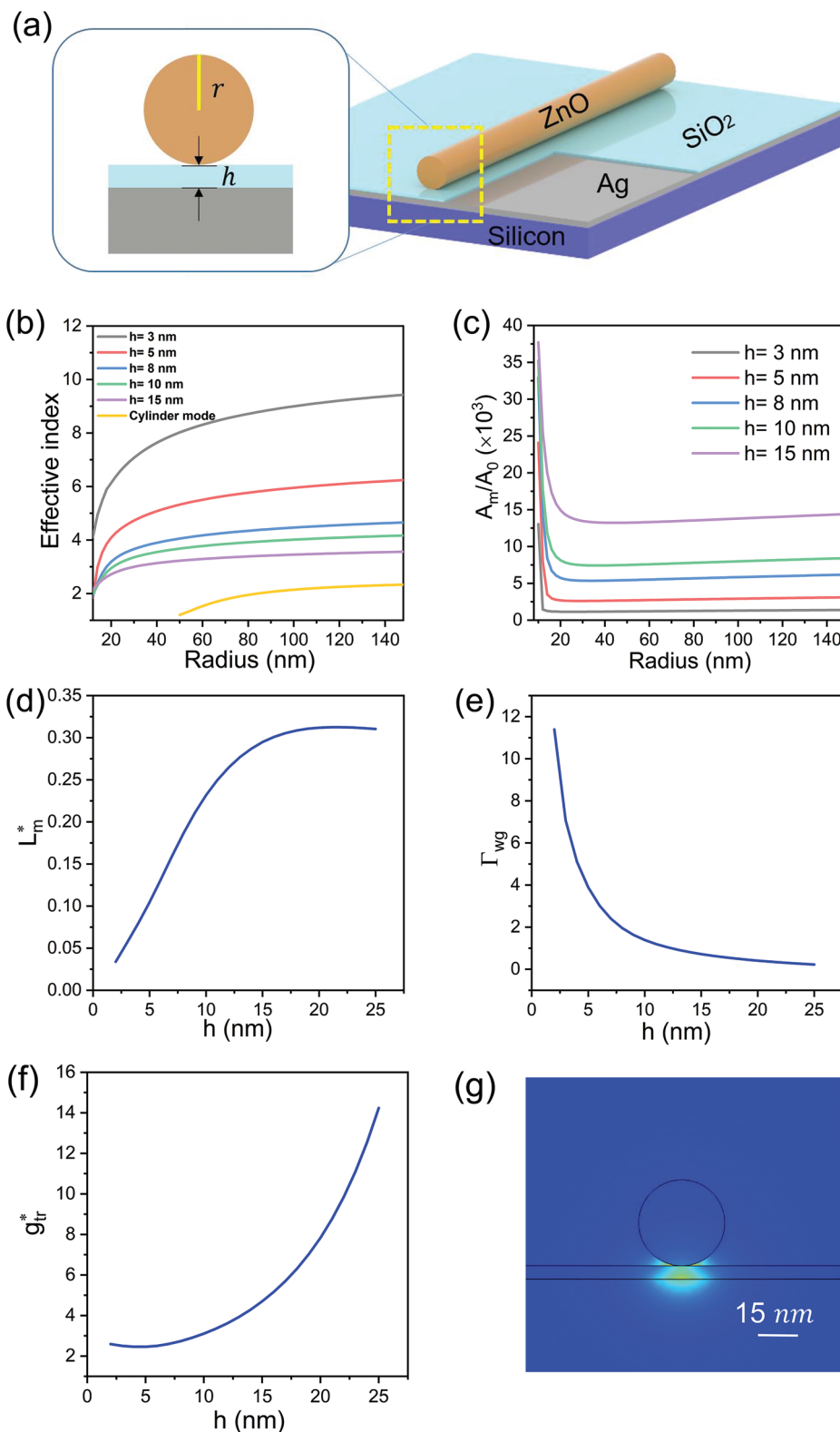


**Figure 4.** a) Schematic diagram of ZnO plasmonic nanocavity. Characteristic diagram of fundamental modes in plasmonic nanocavities with different insulator thickness. b) Effective index; c) Effective modal area; d) Propagation length ( $d = 15$  nm); e) Confinement factor ( $d = 15$  nm). f) Transparency gain of plasmonic nanocavity with different insulator thickness ( $d = 15$  nm). g) Field distribution with  $h = 5$  nm ( $d = 15$  nm).

waveguide mode. When the insulator thickness is decreased, the higher effective index can be observed, indicating the better optical field confinement, thus, leading to the smaller modal area. The modal area  $A_m$  is an indicator of how effectively the material gain can amplify a mode that extends beyond the nanowire.<sup>[108]</sup>

$$A_m = \frac{W_m}{\max\{W(r)\}} = \frac{1}{\max\{W(r)\}} \int_{-\infty}^{\infty} W(r) d^2r \quad (11)$$

Here,  $W_m$  and  $W(r)$  are the electromagnetic energy and energy density, respectively. Due to the coupling between the SP mode and the waveguide mode, hybrid mode is formed and mainly concentrated in the insulator, thus the modal area of the hybrid mode is influenced by the thickness of the insulator. Figure 4c illustrate that the thinner insulator thickness can confine the electric field energy more effectively, resulting in the decrease of mode area. In addition, with the decrease of radius, the mode area first decreases and then increases, and the mode area is the minimum at radius  $\approx 15$  nm. In contrast, for a thinner insulator, the field distribution of the hybrid modes is closed to the metallic and gain region, leading to the enhancement of the modal loss  $\alpha = 2\text{Im}\{k_{hyb}(r, h)\}$ , which reduces the propagation length  $L_m$ .<sup>[108]</sup>

$$L_m = 1 / (2\text{Im}\{k_{hyb}(r, h)\}) \quad (12)$$

$k_{hyb}(r, h)$  is the propagation constant of the hybrid mode. Obviously, it needs to balance with optical confinement and optical loss in SIM waveguide. Therefore, transparent gain  $g_{tr}^*$  is introduced. The definition of  $g_{tr}^*$  is the gain for which energy can travel through the SIM waveguide without dissipation.

$$g_{tr}^* = (L_m^* \Gamma_{wg})^{-1} \quad (13)$$

$L_m^* = L_m / \lambda$  is the normalized propagation length.  $\Gamma_{wg}$  is the waveguide confinement factor of the SIM structure, which indicates the overlapping of the portion of a mode with the gain medium. It can be defined in as follows:

$$\Gamma_{wg} = \frac{\frac{n_a}{2\eta_0} \int_{A_a} d\rho |E(\rho)|^2}{P_z} \quad (14)$$

$P_z$  is the power flow in the propagation direction;  $n_a$  is the refractive index of the gain medium;  $A_a$  is the region of the gain medium;  $\eta_0 = \sqrt{\epsilon_0 \mu_0}$  is the intrinsic impedance,  $\epsilon_0$  and  $\mu_0$  are vacuum permittivity and vacuum permeability, respectively. The thin insulator thickness  $h$  makes the waveguide mode of the nanowire more strongly coupled with the surface plasmon mode of the planar structure, and thus has a better confinement effect on the fundamental mode. The smaller the insulator thickness  $h$ , the closer the field distribution of the hybrid mode is to the metal and gain regions, leading to the decrease of the propagation length and the increase of the confinement factor, as shown in Figure 4d,e. In order to balance between the propagation length and confinement factor, a suitable insulator thickness must be chosen by the transparent gain. As shown in Figure 4f, the minimum transparent gain of the fundamental mode at  $h = 5$  nm can be determined. As shown in Figure 4g is the electromagnetic field distribution of fundamental mode in plasmonic nanocavity.

### 3.3. Purcell Effect

The strong interactions between the gain medium and nanocavity modes results in modified dynamics enhanced known as the Purcell effect.<sup>[109,110]</sup> The Purcell factor  $F_p$  quantifies the rate of energy exchange between the coupled system and the optical mode.

$$F_p = \gamma_\tau / \gamma_0 \quad (15)$$

$\gamma_\tau$  is the enhanced rate of spontaneous emission;  $\gamma_0$  is the natural rate of spontaneous emission. In plasmonic nanolaser, Purcell factor change spontaneous emission. Similarly, it modified spontaneous emission coupling factor  $\beta$ . The Purcell factor  $F_p$  is relationship between  $V_m$  and quality factor  $Q$ .

$$F_p = \frac{3}{4\pi^2} \frac{Q}{V_m} \left(\frac{\lambda}{n_r}\right)^3 \quad (16)$$

Here,  $n_r$  is refractive index of semiconductor material in background environment;  $V_m$  is the effective mode area of cavity; Quality factor  $Q$  denote the photon loss rate of cavity  $\gamma$ . For the Fabry-Perot (FP) mode,<sup>[111]</sup>

$$\gamma = \frac{1}{\tau_p} = \nu(\omega) \left[ \alpha + \frac{1}{2L} \ln\left(\frac{1}{R^2}\right) \right] \quad (17)$$

$$\frac{1}{Q} = \frac{1}{\tau_p \omega} = \frac{\nu(\omega)}{\omega} \left[ \alpha + \frac{1}{L} \ln\left(\frac{1}{R}\right) \right] = \frac{1}{Q_{abs}} + \frac{1}{Q_{mir}} \quad (18)$$

$$\frac{1}{Q_{abs}} = \frac{\nu(\omega) \alpha}{\omega} \quad (19)$$

$$\frac{1}{Q_{mir}} = \frac{\nu(\omega)}{\omega} \frac{1}{L} \ln\left(\frac{1}{R}\right) \quad (20)$$

Here,  $\tau_p$  is the photon life time;  $\nu(\omega) \simeq (\partial \text{Re}[k_z] / \partial \omega)^{-1}$  is the group velocity; the second part in the square brackets of Equation (21) is mirror loss (radiation loss) ( $L$  is the cavity length; and  $R$  is the reflectivity of end facet, and  $R = (n_{hyb}(r, h) - 1)^2 / (n_{hyb}(r, h) + 1)^2$  for plasmonic nanolaser).

### 3.4. Lasing Threshold

At very small physical dimensions, only a few modes exist in the frequency range of interest, and often only one or a few modes can reach the laser threshold conditions. Plasmonic nanolasers also largely exhibit the properties possessed by photonic nanolasers. To simplify the analysis, we only treated one laser mode in the plasmonic nanocavity and the exciton distributed uniformly in the nanowire after the laser excitation.<sup>[112]</sup> In this case, the rate equations for single laser mode are sufficient to describe spaser behavior.

$$\frac{dn}{dt} = \eta p - \gamma_\tau n - \beta \Gamma \gamma_\tau s (n - n_0) \quad (21)$$

$$\frac{ds}{dt} = \beta \gamma_\tau n + \beta \Gamma \gamma_\tau s (n - n_0) - \gamma s \quad (22)$$

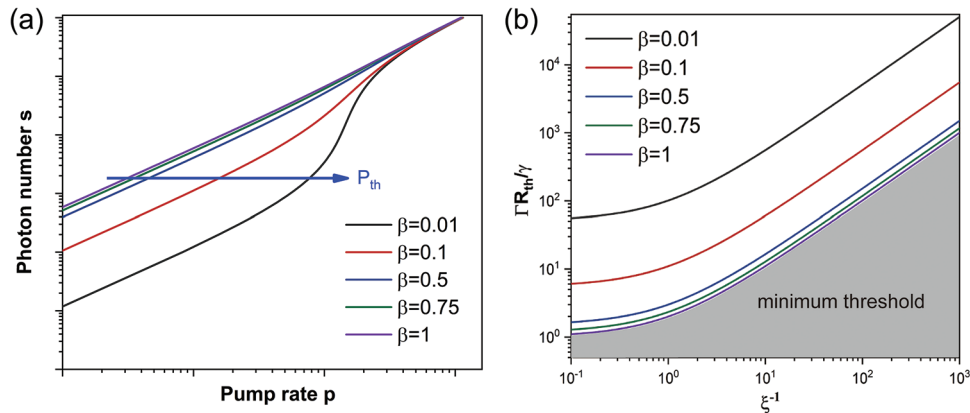


**Figure 5.** a) Light-pump curves with different  $\beta$ . b) Normalized threshold as a function of the  $\zeta$  and  $\beta$  parameters.

The rate equation can be described by the changing rates of the exciton density  $n$  and the photon density  $s$ , containing various contribution and dissipation terms. Here,  $\eta$  is the paroportion of pump power absorbed by gain medium in laser;  $p$  is the pumping power rate;  $\gamma_\tau = \frac{1}{\tau_0}$  is the spontaneous emission rate;  $\Gamma$  is the overlap factor between the optical mode and the gain region;  $\gamma_g = \beta\Gamma\gamma_\tau s n_0$  is the absorption rate caused by the gain medium;  $n_0$  is the carrier density when the gain medium is transparent.<sup>[113]</sup>

The purpose of laser miniaturization is to reduce power consumption. The physically small size of the laser device has few optical modes available to the gain medium, which increases  $\beta$ . For simplified analysis in static conditions, we estimated that  $F_p = 5$ ,  $n_0 = 0$ , and  $\Gamma = 1$ . Finally, as shown in **Figure 5a**, we can plot the light-pump curves with different  $\beta$ . It can be seen that the threshold increases as  $\beta$  increases. Because the larger  $\beta$  allows for the initiation of excited radiation at weaker pump conditions, resulting in lower laser threshold. But is it enough to just change the size if we want to achieve low-threshold plasmonic nanolasers? The threshold is defined as the condition in which the rates of spontaneous and stimulated emission into the laser mode are equal. Under static conditions, through the analysis and solution of Equations (21) and (22), the threshold photon density pump rate  $P_{th}$  (photon density pump rate  $P = phv/A$ ) can express using the following;

$$P_{th} = \frac{h\nu}{\eta A} \frac{(1 + \beta)}{2} \left[ \frac{\gamma}{\beta\Gamma} + F_p \frac{2n_0 V_{phy}}{\tau_0} \right] \quad (23)$$

$h\nu$  is the photon energy of the emission;  $A$  is the area of the pump beam;  $\Gamma$  is the overlap factor between the optical mode and the gain region;  $V_{phy}$  is the physical volume of gain medium. By simplifying Equation (23), it can be obtained an expression for the threshold rate of photon generation.

$$R_{th} = \frac{\gamma}{2\Gamma} \left( 1 + \frac{1}{\beta} \right) \left( 1 + \frac{1}{\zeta} \right) \quad (24)$$

where  $R_{th} = \eta P_{th} A / h\nu$ ; the definition of  $\Gamma R_{th} / \gamma$  is a normalized threshold pump rate.  $\zeta = \gamma \tau_0 / (\beta F \Gamma n_{inv} V_{phy})$  is the ratio of cavity loss to material loss, which is an important parameter for characterizing the threshold of nanolaser;  $F$  is the Purcell factor;  $n_{inv} = 2n_0$  is the carrier density at twice the transparency value. Espe-

cially, the minimum pump rate,  $R_{th} = \gamma / \Gamma$ , indicates that photons must be supplied to the cavity as fast as they are being lost.<sup>[114]</sup>

From **Figure 5b**, it can be seen that there are two ways to reduce the threshold value: One is to increase  $\beta \rightarrow 1$ , which means small size and strong Purcell effect; the other one is to increase  $\zeta$ , which indicates that cavity loss should be dominant. But  $\zeta$  and  $\beta$  are not unrelated, cavity loss and material loss are also related. Despite inevitably increase of total cavity loss with laser miniaturization, plasmonic nanolasers can reduce the total cavity loss by hindering radiation loss via the plasmonic field confinement effect. Hence, when an equilibrium point is reached between the cavity loss and material loss, the threshold can be minimized. Wang et al. studied the gain and loss in the CdSe plasmonic laser as an example (**Figure 6a**).<sup>[115]</sup> As shown in **Figure 6b**, gain material loss, metallic loss and radiation loss in plasmonic laser was determined. And it further provided dependece relationships between loss and gain. Obviously, using of High quality gain material and plasmonic material are vital for the development of low threshold plasmonic nanolasers.

## 4. Experimental Demonstrations of Plasmonic Nanolaser

The inherent high loss in surface plasmon resonance give a great challenge to the experimental implementation of spaser. In 2009, three groups realized three different configurations of plasmonic lasers.<sup>[30–32]</sup> Moreover, each group demonstrated that plasmonic lasers exhibit subwavelength confinement in different dimensions. The spaser designed by Noginov et al. includes a gold NPs core as plasmon resonator, and dielectric nanoshell containing dye molecule. This spaser is the smallest coherent generator to date, ranging in size from a few nanometers to tens of nanometers.<sup>[30]</sup> Oulton et al. reported a plasmonic nanowire nanolasers with metal-insulator-semiconductor (MIS) structure, hybridized plasmon modes propagate along the nanowires.<sup>[31]</sup> Hill et al, reported electrically pumped lasing in metal-insulator-metal (MIM) sub-wavelength plasmonic waveguides.<sup>[32]</sup> In terms of physical mechanisms, these plasmonic nanolasers and spaser are essentially the same, the only difference being whether the local or propagating plasmon mode is coupled to the gain material. And these plasmonic nanolasers are highly compact coherent light sources with ultrafine dynamics and a wide range of

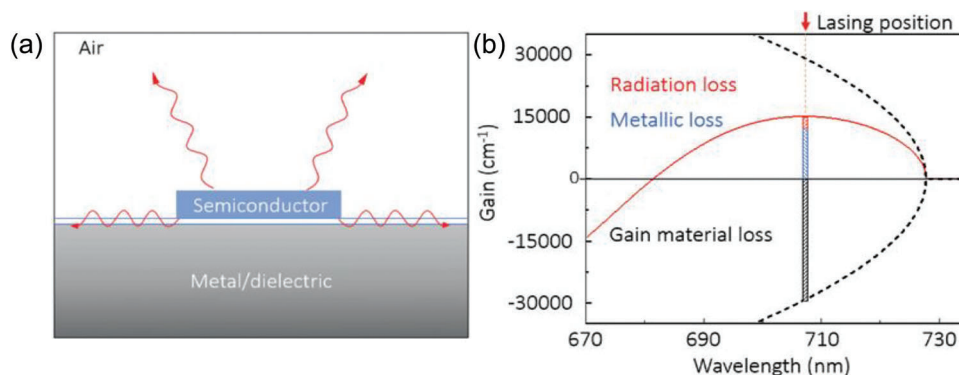


**Figure 6.** a) Schematic of CdSe plasmonic nanolaser. b) The relationship with loss and gain at full lasing state. a, b) Reproduced with permission.<sup>[115]</sup> Copyright 2020, De Gruyter.

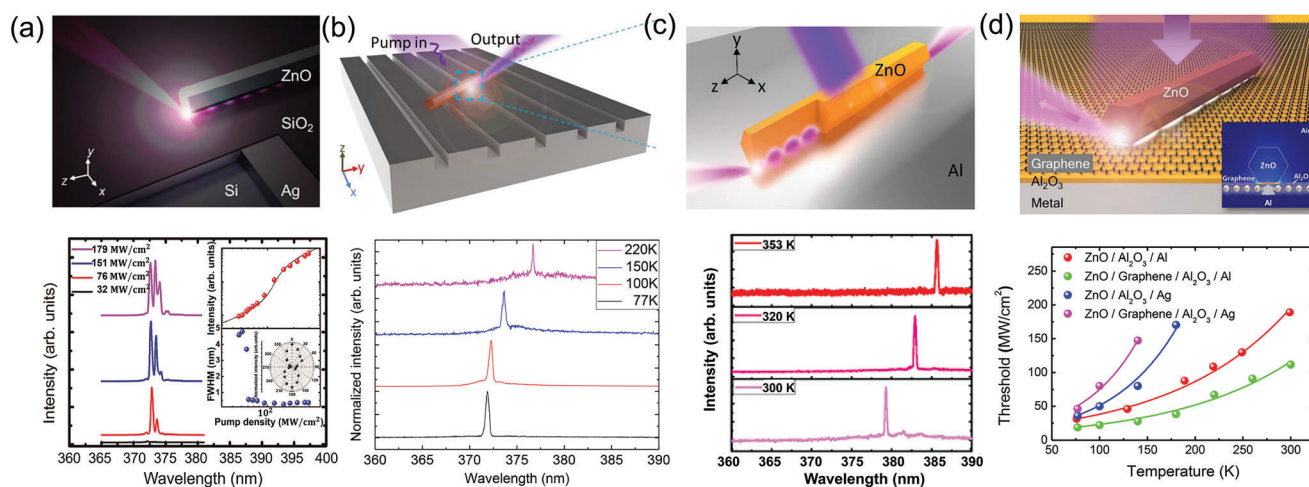


**Figure 7.** a) Upper panel: Schematic diagram of ZnO plasmonic nanolaser. Lower panel: Evolution of the lasing spectra at a temperature of 77 K; Inset: threshold curve, the line width of the emission peak versus the pumping power density and the corresponding polar plot of the emission intensity. Reproduced with permission.<sup>[136]</sup> Copyright 2015, ACS. b) Upper panel: Schematic diagram of pseudowedge SPP nanolaser. Lower panel: Lasing spectra of pseudowedge SPP nanolasers with the temperature increasing up to 220 K. Reproduced with permission.<sup>[137]</sup> Copyright 2018, ACS. c) Upper panel: Schematic diagram of ZnO/Al film SPP nanolaser. Lower panel: laser spectra measured from 300 to 353 K. Reproduced with permission.<sup>[138]</sup> Copyright 2016, ACS. d) Upper panel: Schematic of GIM plasmonic nanolaser. Lower panel: The threshold of four types of plasmonic nanolaser measured at different temperature. Reproduced with permission.<sup>[139]</sup> Copyright 2019, ACS.

application prospects. By changing gain medium, low threshold plasmonic nanolaser obtained by high-quality cavity, well-defined contact interface, effective modal coupling achieve laser emission from ultraviolet (UV) to Infrared (IR).<sup>[116–133]</sup>

## 4.1. Optically Pumped Plasmonic Nanolaser

### 4.1.1. Ultraviolet Band

In aspect of UV plasmonic nanolasers, Oulton et al. in 2014 demonstrated plasmonic ZnO nanowire laser under pulse excitation of less than 150 fs.<sup>[134]</sup> The ZnO exciton is located near the SP frequency in this Ag-based plasmonic nanolaser, accelerating exciton recombination compared to ZnO photonic nanolasers at room temperature. However, fast recombination rate in plasmonic devices (diameter less than 120 nm) hinder the build-up

of a population inversion in this work, resulting in no lasing behavior in diameter less than 120 nm nanowire.

In addition to ZnO, GaN is also an ideal material for UV lasers. Zhang et al. proposed a very low threshold (3.5 MW cm<sup>-2</sup>) GaN plasmonic laser at room temperature.<sup>[135]</sup> The using of a thin Al film with a roughness of 0.359 nm greatly reduces ohmic losses at the interface. More importantly, the exciton-SP energy transfer is effectively improved, thus providing sufficient optical gain energy to compensate for the loss.

The above works are obviously far from the original goal of achieving highly compact plasmonic nanolaser. The researchers did not stop their research on plasmonic nanolasers. With the upgrade of instruments, the optimization of detection efficiency and the addition of excellent single crystal metals, UV plasmonic lasers have made great breakthroughs.

In 2015, as shown in Figure 7a, a sharp laser pattern with a peak at 373 nm was observed in ZnO MIS structures with

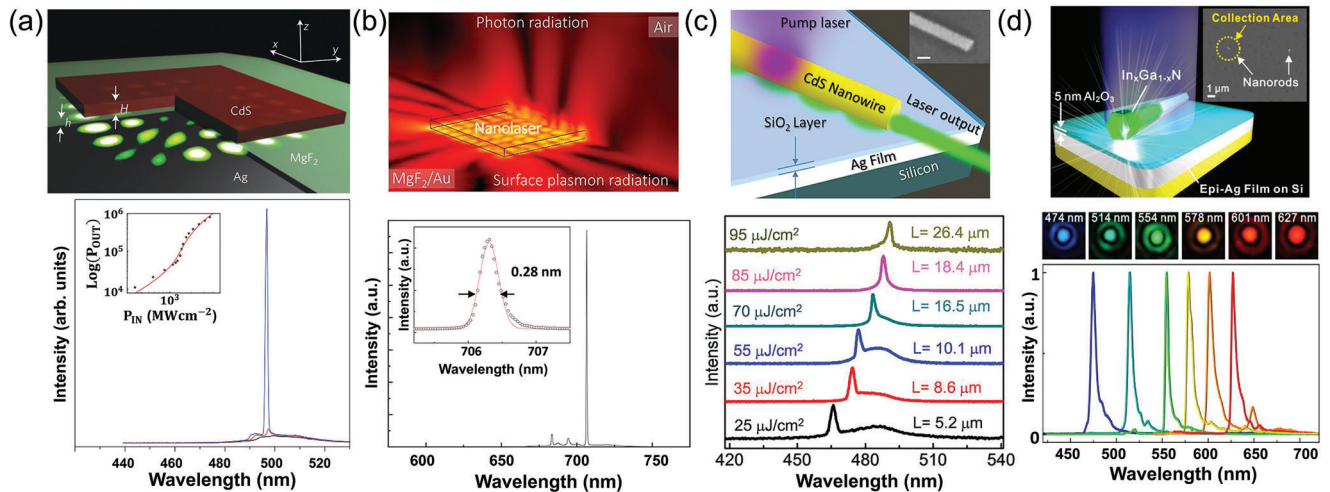


**Figure 8.** a) Upper panel: Schematic diagram of CdS plasmonic laser at room temperature. Lower panel: Power-dependent laser spectra and integrated light-pump response (inset). Reproduced with permission.<sup>[140]</sup> Copyright 2011, NPC. b) Upper panel: Radiations field of CdSe plasmonic nanolasers. Lower panel: The room-temperature laser spectra at a peak pump power of  $3.6P_{th}$ . single mode lasing of 0.28 nm line width (inset). Reproduced with permission.<sup>[141]</sup> Copyright 2018, ACS. c) Upper panel: Schematic diagram of CdS plasmonic nanolaser structure. The SEM image shows a representative plasmonic nanolaser with a scale of 100 nm (inset). Lower panel: The laser spectra (with different excitation power) measured on CdS nanowires of different lengths ( $\approx 110 \pm 10$  nm in diameter). Reproduced with permission.<sup>[142]</sup> Copyright 2017, ACS. d) Upper panel: Schematic diagram of nanolaser structure. SEM image at top right. Lower panel: A full-color, single-mode laser image observed from a single nanorod with an emission linewidth of  $\approx 4$  nm. Reproduced with permission.<sup>[143]</sup> Copyright 2014, ACS.

side lengths 15 nm of ZnO nanowire.<sup>[136]</sup> A UV ZnO plasmonic nanolaser with an effective mode volume of  $< \lambda^3/1000$  has been realized. This record was later broken by the pseudowedge plasmonic nanolaser with a ZnO nanowire placed on a Ag grating, as shown in Figure 7b.<sup>[137]</sup> It exhibits ultracompact performance, which its effective mode volume is 100 times smaller than that of a planar SP nanolaser. But these devices can only operate at 77 K if they want to achieve other beneficial performance. Subsequently, the group demonstrated that Al-based ZnO plasmon nanolasers still realizes single-mode emission at high temperature of 353 K. And plasmonic nanolaser with Purcell factor of 16.5 show low threshold laser performance (Figure 7c).<sup>[138]</sup> In order to pursue the plasmonic nanolaser with lower threshold, ZnO/graphene/insulator/metal layer (GIM) structure has been constructed, as shown in Figure 7d, which can affect the dispersion characteristics of SPs and eliminate the fixation limitations of plasmon metal.<sup>[139]</sup> Due to the difference in Fermi levels, graphene changes the electron density on the metal surface. The electron density on Al surface increases in GIM structure, leading to the blue shift of Al plasmon frequency. In contrast, the threshold of ZnO nanowire laser on the Al-based GIM structure is reduced by 50%, while the Ag-based GIM structure shows completely opposite effect.

#### 4.1.2. Visible Band

In the visible band, CdS nanowires or nanosheets, InGaN@GaN nanowires, perovskite nanowires can also be applied to achieve plasmonic nanolasers. In 2011, as shown in Figure 8a, Ma et al. proposed a room-temperature CdS nanosheet-insulator-metal by utilizing total internal reflection of SP to reduce radiation loss.<sup>[140]</sup> Compared to FP resonance hybridization mode, total in-

ternal reflection resonance hybridization mode generating from 5 nm of nanogap could lead to high Q ( $\sim 100$ ) and strong mode confinement ( $\lambda/20$ ). By controlling the size of CdS, the number of cavity modes can be reduced, and the output of single mode laser can be operated. And lasing threshold in single-mode laser is  $1096 \text{ MW cm}^{-2}$  in the room-temperature. Laser with small physical volumes can reduce power consumption. However, with reducing the cavity, the material loss will inevitably increase and the external quantum efficiency will decrease. High quality gain materials with hindered nonradiative channel are effective manner to decrease material loss and improve the external quantum efficiency. Plasmonic nanolasers with extremely low thresholds of  $10 \text{ KW cm}^{-2}$  at room temperature has been demonstrated by using high crystal quality CdSe nanosquares as the gain material (Figure 8b).<sup>[141]</sup>

The loss caused by the change of size also affects the emission wavelength of the laser. As shown in Figure 8c, plasmonic nanolaser with stable emission from 465 to 491 nm wavelengths has been demonstrated by adjusting the length of CdS nanowires with the inherent self-absorption.<sup>[142]</sup> In addition, single-mode plasmonic lasing in the visible waveband has also been achieved by gain-composition-tunable. Individual  $\text{In}_x\text{Ga}_{1-x}\text{N}$ @GaN core-shell nanorods were dispersed on a high quality silver film covered with  $\text{Al}_2\text{O}_3$  (Figure 8d).<sup>[143]</sup> And the threshold of CW laser is successfully reduced to ultra-small values in the three primary colors, and the possibility of “thresholdless” lasing behavior of blue plasmonic nanolaser is demonstrated. Importantly, these studies provide a new way for wavelength adjustable plasmonic nanolasers.

In recent years, perovskite has become one of the remarkable materials due to its excellent optical and electrical performance.<sup>[144–146]</sup> The chemical structure  $\text{ABX}_3$  of perovskite: A is a monovalent cation, B is a divalent metalion, and X is

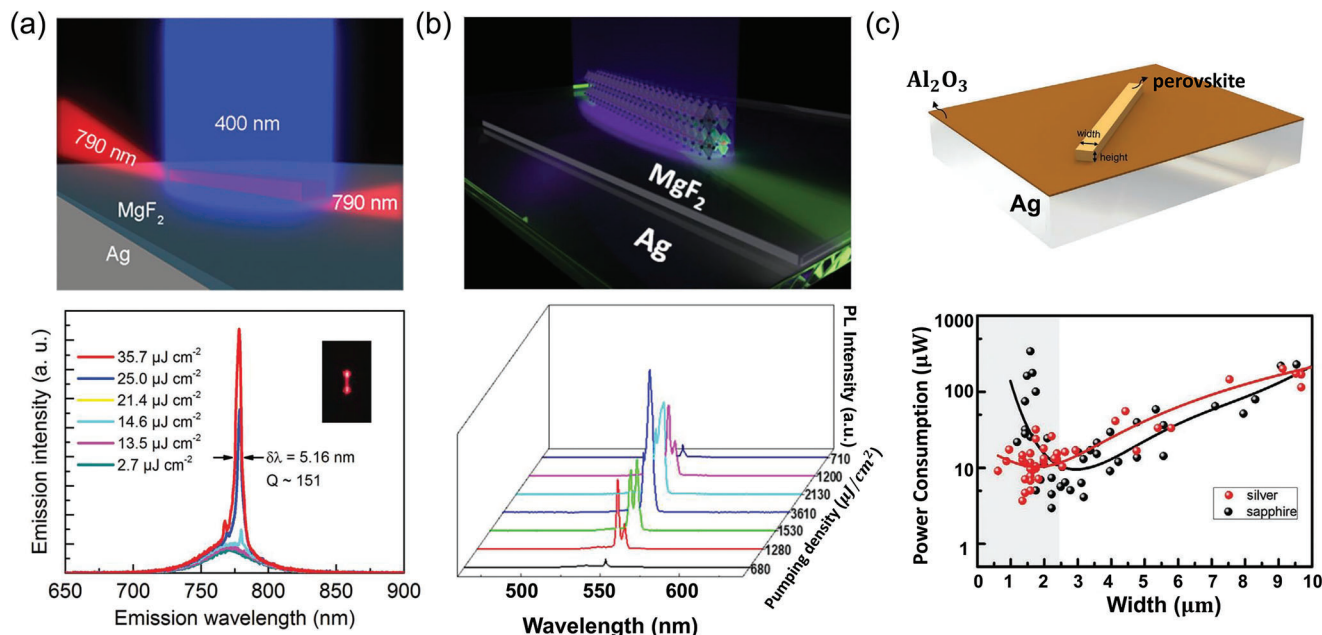


**Figure 9.** a) Upper panel: Schematic diagram of CH<sub>3</sub>NH<sub>3</sub>PbI<sub>3</sub> plasmonic nanolaser. Lower panel: Power-dependent photoluminescence (PL) spectra. The inset shows the optical image of laser equipartition excitation nanowires. Reproduced with permission.<sup>[147]</sup> Copyright 2016, RSC. b) Upper panel: Schematic diagram of CH<sub>3</sub>NH<sub>3</sub>PbBr<sub>3</sub> plasmonic nanolaser. Lower panel: Emission spectra with different pumping intensities. Reproduced with permission.<sup>[148]</sup> Copyright 2019, Wiley-VCH. c) Upper panel: Schematic diagram of plasmonic nanolaser based on the structure of CH<sub>3</sub>NH<sub>3</sub>PbBr<sub>3</sub>/Al<sub>2</sub>O<sub>3</sub>/Ag. Lower panel: Threshold power consumption statistics of perovskite nanowires with different scales. Reproduced with permission.<sup>[149]</sup> Copyright 2022, Wiley-VCH.

a halide. Because of its adjustable composition, simple preparation process and low cost, it offers great scope for practical applications. In addition, high quantum efficiency and exciton binding energy make it highly advantageous as a laser. A lot of researches on perovskite plasmonic nanolasers have been reported subsequently. As shown in Figure 9a, Yu et al. introduced the plasmonic laser with single-crystalline organic-inorganic CH<sub>3</sub>NH<sub>3</sub>PbI<sub>3</sub> nanowires as gain material.<sup>[147]</sup> The device achieves a relatively low threshold at room temperature (13.5 μJ cm<sup>-2</sup>), and the devices operate well even at temperatures as high as 43.6 °C. This demonstration highlights that perovskite materials can achieve high optical gain for plasmonic nanolaser.

As shown in Figure 9b, plasmonic nanolaser based on the CH<sub>3</sub>NH<sub>3</sub>PbBr<sub>3</sub> nanowire/dielectric layer/metal was fabricated by replacing iodine in perovskite with bromine.<sup>[148]</sup> The plasmonic nanolasers realize the excellent performance of a low threshold of 62 μJ cm<sup>-2</sup>. Interestingly, the plasmonic nanolaser can achieve single-mode to multi-mode conversion by simply adjusting the injection energy. According to the mode characteristics of plasmonic nanolaser, the performance of the nanolaser is affected by the cavity size. Therefore, in order to obtain the low-threshold plasmonic nanolaser, it is also necessary to establish the law between the cavity size of perovskite and the threshold power consumption of perovskite. By a series of rigorous measured methods, the scaling laws for plasmonic CH<sub>3</sub>NH<sub>3</sub>PbBr<sub>3</sub> nanowire lasers are expounded. As shown in Figure 9c, when the width of CH<sub>3</sub>NH<sub>3</sub>PbBr<sub>3</sub> is less than 2.5 μm, the hybrid plasmonic CH<sub>3</sub>NH<sub>3</sub>PbBr<sub>3</sub> nanolasers exhibits low power consumption.<sup>[149]</sup>

#### 4.1.3. Infrared Band

For the application in the field of information equipment and communication technology, the plasmonic nanolasers have made progress in the infrared band. In 2010, Kwon et al. successfully demonstrated a subwavelength plasmonic nanolaser in the infrared band. As shown in Figure 10a, the top of the InP nanodisk was glued to a transparent glass substrate, and the bottom and side walls of the nanodisk were coated with Ag. Four InAsP QWs are embedded in the middle of the nanodisk.<sup>[150]</sup> The lasing threshold in plasmonic nanolaser with mode volume of  $0.56(\lambda/2n)^3$  ( $n$  is refractive index) is  $\approx 120$  kW cm<sup>-2</sup> at a temperature of 8K.

In the infrared region, the basic confinement capacity of plasmonic device is accompanied by serious ohmic losses, which obviously degrade their performance. Therefore, people have long sought plasmon materials with lower losses than noble metals in the infrared region. As shown in Figure 10b, research has found that sodium-based plasmonic devices had the most stable and excellent performance in the near-infrared wavelength region.<sup>[151]</sup> A high quality sodium film with an electronic relaxation time of 0.42 picoseconds was prepared by thermal assisted spinning coating process. In a direct waveguide experiment, 200 μm propagation length of SP supported on the sodium-quartz interface demonstrated that sodium film has low ohmic loss in the near infrared wavelength. And it is further demonstrated sodium-based plasmonic nanolaser has a low laser threshold of 140 KW cm<sup>-2</sup> in the room temperature. At room temperature, these sodium-based plasmonic device packaged by epoxy exhibited stable performance after several months.

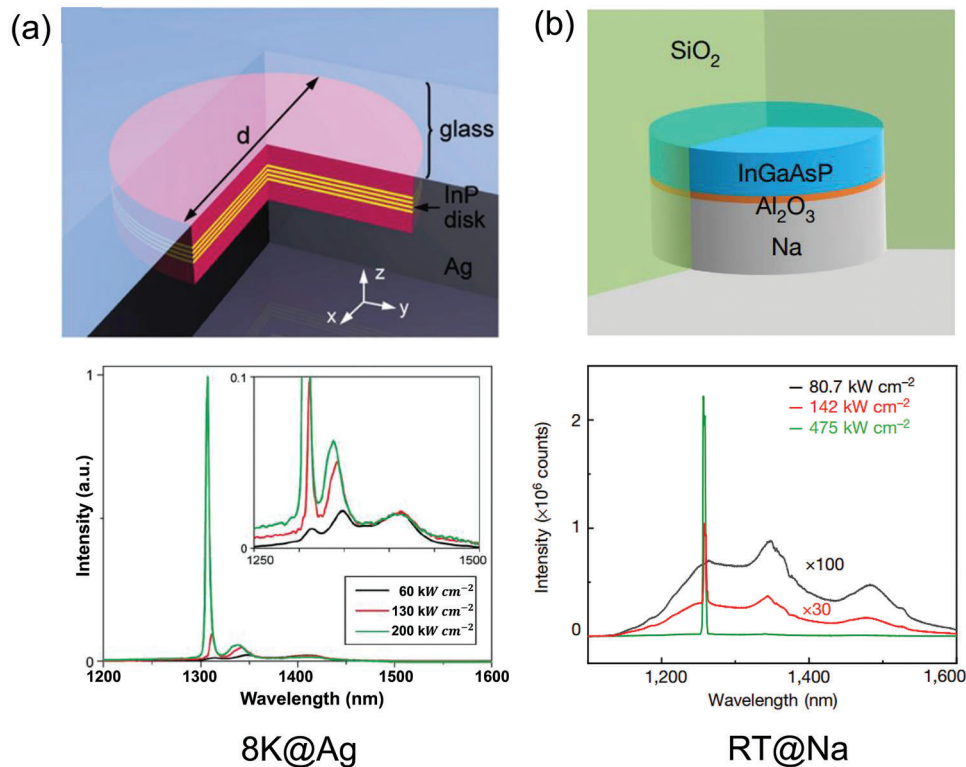


**Figure 10.** a) Upper panel: Schematic diagram of the plasmonic nanocavity. Lower panel: Measured PL spectra at different absorbed peak pump intensities at 8 K. The inset shows the corresponding magnification spectra. Reproduced with permission.<sup>[150]</sup> Copyright 2010, ACS. b) Upper panel: Room-temperature sodium-based plasmonic nanolaser. Lower panel: PL spectra of the sodium-based plasmonic nanolaser. Reproduced with permission.<sup>[151]</sup> Copyright 2020, NPG.

These works demonstrate that the performance of sodium-based plasmonic device is greatly improved compared with that of plasmonic device using noble metals.

#### 4.2. Electrically Pumped Nanolaser

Optical pumping is a convenient way to study the laser operating mechanism, while electrical pumping is a necessary path for plasmonic devices to move toward practical applications. Because of the large metal loss and radiation loss in the metal cavity, initially electrically driven nanolasers mainly operate at low temperature.<sup>[32,152–155]</sup> With the development of nanoscience and technology, high performance electrically pumped nanolaser at room temperature has been gradually realized.<sup>[38,156–158]</sup>

In 2007, Hill et al. first reported laser emission within an electrically pumped metal-clad nanocavity. The nanocavity is formed by semiconductor heterojunction covered by Au film, and electrons are injected through the top of the Au column.<sup>[152]</sup> And this structure achieves the excellent performance of small size, low power and high speed. Although dielectric mode rather than plasmonic mode exists in the device, this method provides the possibility for the realization of electric pumped plasmonic nanolaser. In 2009, Hill group realized electrically pumped plasmonic nanolaser in an MIM subwavelength plasmonic waveguide nanocavity.<sup>[32]</sup> The waveguide mode is constrained by 1D

plasmonic mode between metal walls and coupled to gain materials (InGaAs). In the following years, metal-covered nanocavity structures have realized breakthroughs from low to room temperature, providing technical and theoretical support for electric pumped plasmonic nanolaser.

In 2011, Ding et al. realized the electric pump laser output in an Ag-encapsulated subwavelength semiconductor core at a temperature of 260 K.<sup>[153]</sup> The laser with a physical cavity volume of  $0.96\lambda^3$  ( $\lambda = 1563.4 \text{ nm}$ ) is shown. In 2012, as shown in **Figure 11c**, at room temperature, laser emission further has been realized in electrically pumped subwavelength metal cavities.<sup>[154]</sup> The volume of the nanolaser can be as small as  $0.42\lambda^3$  ( $\lambda = .55 \mu\text{m}$ ). The same year, Ding group<sup>[155]</sup> realized the electric pump laser output in metal-insulator-semiconductor-insulator-metal subwavelength semiconductor nanocavity. The laser with a physical cavity volume of  $0.19\lambda^3$  is shown at a temperature of 100 K. Although metal cavities can confine light to a volume much smaller than the operating wavelength, laser operation is still prohibited by the cavity self-heating at room temperature (including to junction and heterojunction heating, Joule heating, and non-radiative recombination heating). Similarly, for electrically pumped plasmonic nanolasers, lasing operation at room temperature is also a great challenge. And due to the limitation of microfabrication technology, the laser emission of the electrically pumped plasmonic nanolaser is in the infrared region. In 2019, Yang et al.<sup>[159]</sup> first designed and implemented an

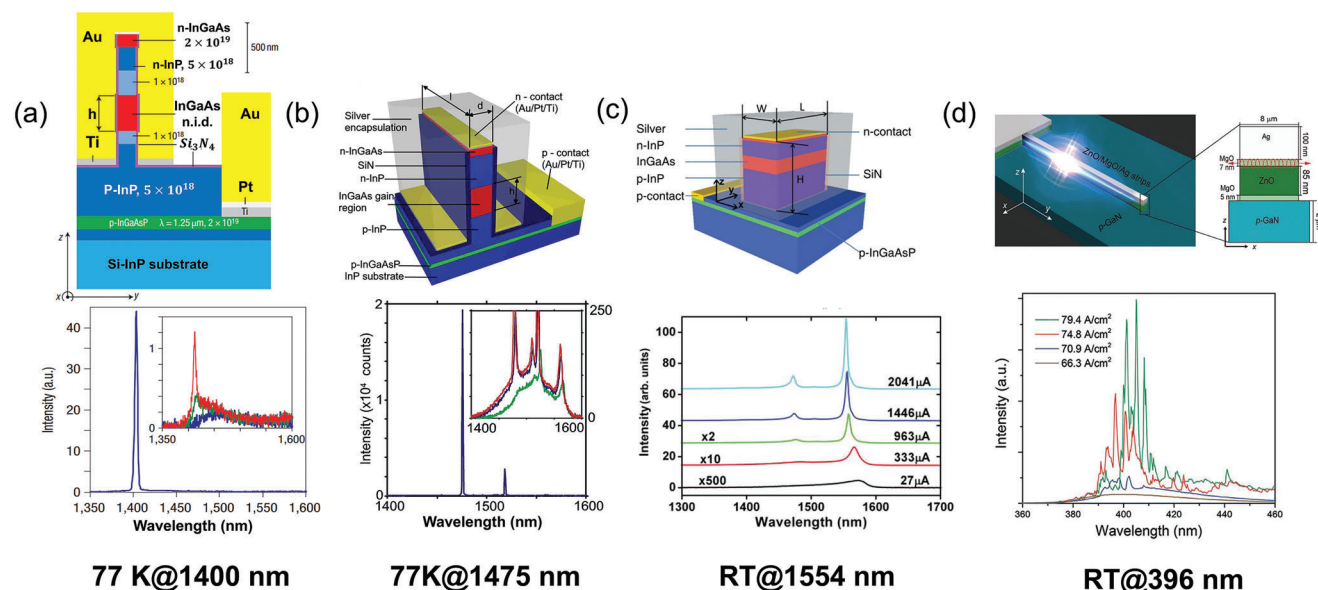


**Figure 11.** a) Upper panel: Schematic diagram of device structure. Lower panel: The laser spectrum was measured with a pump current of 60  $\mu$ A. Inset: emission spectra of different current at 77 K. Reproduced with permission.<sup>[152]</sup> Copyright 2007, NPG. b) Upper panel: Schematic diagram of the electrically driven MIM plasmonic nanolaser. Lower panel: Emission spectra of different injection current density in sub-wavelength plasmonic waveguide. Reproduced with permission.<sup>[32]</sup> Copyright 2009, OSC c) Upper panel: Schematic of the Ag metal-semiconductor nanolaser. Lower panel: Emission spectra under different currents. Reproduced with permission.<sup>[155]</sup> Copyright 2012, APS. d) Upper panel: Schematic diagram of the electrically driven ZnO plasmonic laser. Lower panel: Emission spectra of different injection current density in the plasmonic laser. Reproduced with permission.<sup>[159]</sup> Copyright 2019, Wiley-VCH.

electrically driven ultraviolet plasmonic laser with p-GaN/MgO (electron barrier layer)/ZnO/MgO/Ag structure at room temperature (Figure 11d). The Ag/MgO/ZnO MIS as hybrid plasmonic nanocavity in this device can satisfy strong optical confinement and lower ohmic loss simultaneously. The device reaches very low threshold of 70.2  $\text{A cm}^{-2}$  at room temperature, and the laser output power can reach 30  $\mu$ W at an injection current of 40 mA. Electrically driven UV plasmonic nanolaser at the subwavelength scale may have potential applications in photolithography, sensing, and biomedical applications.

## 5. Application of Plasmonic Laser

In recent years, significant progress has been made in advancing plasmonic nanolasers, which has evolved from initial concepts to a variety of experimental demonstrations. Although the key design problems are still challenges, plasmonic nanolasers have unprecedented opportunities due to constant discovery of the high-gain and low-loss metal, the structure optimized by artificial intelligence (AI) and microfabrication. For example, their intrinsic properties indicate potential applications in optical interconnection,<sup>[34–39]</sup> biochemical analysis,<sup>[41–47]</sup> and far-field application.<sup>[56]</sup>

### 5.1. On-Chip Optical Interconnections

In nanophotonic integrated circuits, subwavelength lasers are an attractive device due to its small size and low energy consumption. In recent years, many efforts have been made for applying plasmonic nanolaser to on-chip optical interconnection.

Ma et al. demonstrated a deep subwavelength waveguide embedded (WEB) plasmonic laser.<sup>[35]</sup> As shown in Figure 12a, five WEB plasmonic laser devices are composed of five silver bands with 1  $\mu\text{m}$  width and CdS band. The device can efficiently convert coherent surface plasmon from a small laser cavity to an embedded photonic semiconductor waveguide, whose radiation efficiency is increased by  $\approx 35\%$ . In addition, as shown in lower panel image of Figure 12a, WEB plasmonic laser can also realize effective electrical modulation and wavelength multiplexing at room temperature. The work achieves the initial interaction between electricity and light in plasmonic nanolaser. At room temperature, ZnO SPP nanowire lasers also are shown to be actively modulated on graphene-insulator-metal (GIM) composite platform (Figure 12b).<sup>[39]</sup> It changes the cavity mode from a standing wave mode to a propagating wave mode at injected current of 100 mA, resulting in an increase of laser threshold and Doppler shift caused by non-reciprocal propagation properties. The above studies indicate that the optical properties of the plasmonic nanolaser can be regulated by electric injection.

Obviously, in order to realize on-chip optical interconnection, the plasmonic laser device also needs to be able to couple effectively with the integrated waveguide. In 2006, waveguide-integrated plasmonic nanocavity sources with physical small footprint 0.06  $\mu\text{m}^2$  applied in on-chip optical interconnection has been investigated in theory (Figure 12c).<sup>[37]</sup> Its emission can transfer  $\approx 60\%$  into planar on-chip waveguides. Further, a metal-cavity light-emitting diode coupled to InP waveguide on silicon has been demonstrated in experiment (Figure 12d).<sup>[39]</sup> The emission characterized by grating coupler has very high external quantum efficiency (EQE). The performance of this device

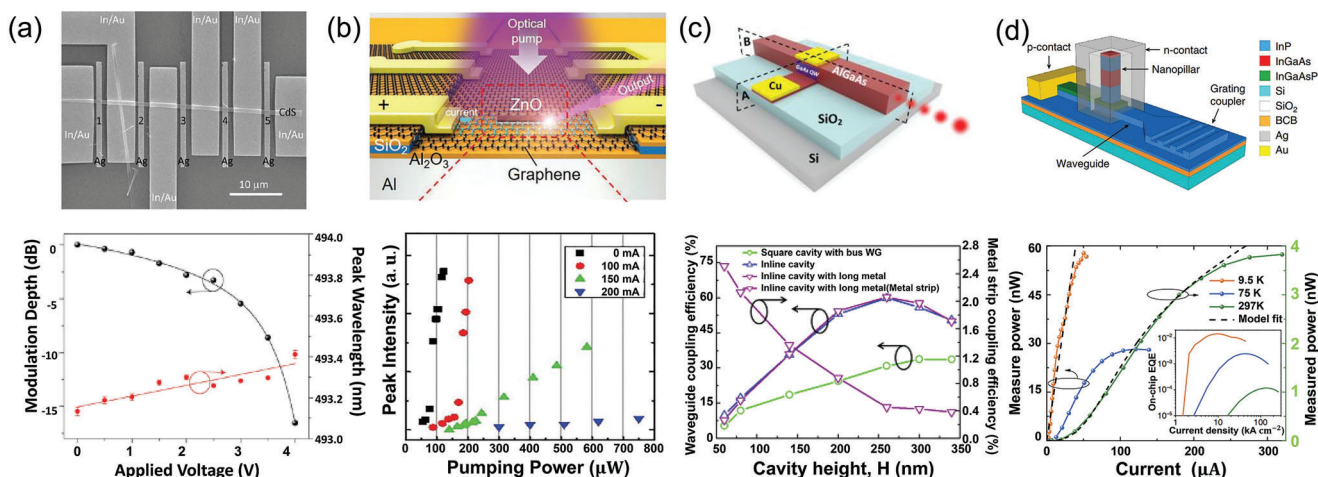


**Figure 12.** a) Upper panel: Plasmonic lasers integrated arrays. Lower panel: Modulation depth (black) and peak wavelength shift (red) under different applied voltage. Reproduced with permission.<sup>[35]</sup> Copyright 2012, ACS. b) Upper panel: Schematic of ZnO plasmonic nanolasers on the GIM structure. Lower panel: Peak intensity of ZnO plasmonic nanolasers on the GIM structure under different current injection conditions of graphene. Reproduced with permission.<sup>[39]</sup> Copyright 2020, Wiley-VCH. c) Upper panel: Schematic of an electric-pumping in-line cavity nanolaser bonded on a SiO<sub>2</sub>/Si substrate. Lower panel: Comparison of coupling efficiency for four-nanolaser plasmon cavities to the neighboring waveguides under different cavity height. Reproduced with permission.<sup>[37]</sup> Copyright 2016, ACS. d) Upper panel: Schematic of the metal-cavity LED on a Si substrate. Lower panel: Light–current characteristics of the nanopillar LEDs at different temperatures. Inset: the calculated EQE versus current density. Reproduced with permission.<sup>[38]</sup> Copyright 2017, NPG.

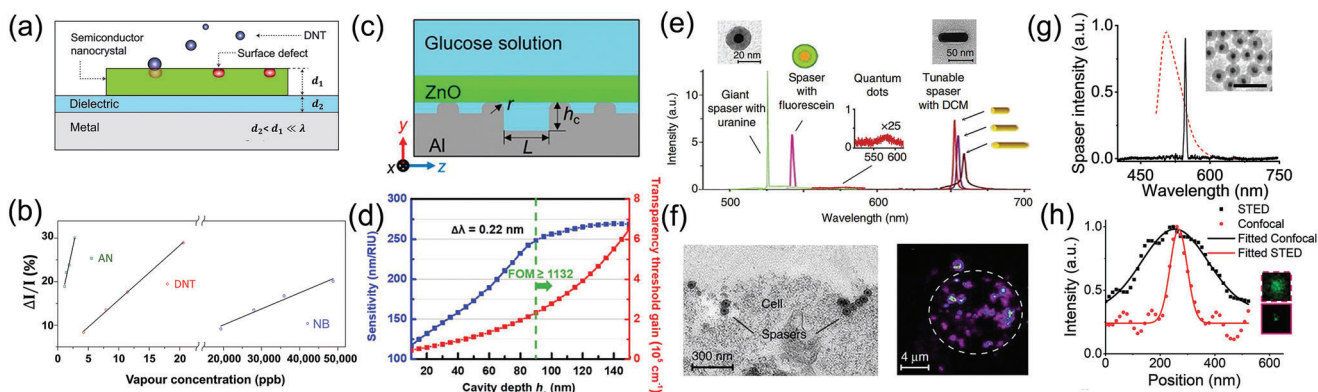


**Figure 13.** a) Schematic of a plasmonic nanolaser sensor for detection of explosives. b) Calibration curves for the three analytes. a, b) Reproduced with permission.<sup>[40]</sup> Copyright 2014, NPG. c) Schematic diagram of the hollow defect plasmonic nanocavity for sensing the glucose solution. d) Sensitivity and transparency threshold gain in a glucose solution. c, d) Reproduced with permission.<sup>[44]</sup> Copyright 2018, ACS. e) TEM of spherical, rod-like spasers and Quantum dots, and their corresponding lasing emission spectra. f) TEM image of spasers on a breast cancer cell membrane (left); photothermal (PT) image of cancer cell labelled with spasers (right). e, f) Reproduced with permission.<sup>[45]</sup> Copyright 2017, NPG. g) Spectra of fluorescent dyes (dash red line) and spaser NPs (solid black line). Inset shows TEM image of spaser. Scale bar, 100 nm. h) PL intensity profile for confocal image and STED image. g, h) Reproduced with permission.<sup>[46]</sup> Copyright 2020, Wiley-VCH.

is much better than that of many waveguide coupled nanoscale light sources under the same conditions.

## 5.2. Biochemical Analysis

Surface plasmon resonance (SPR) effect is currently an important tool for biochemical sensing and detection. However, due to strong radiative and nonradiative damping of metal, the SPR in the visible and near-infrared wavelengths exhibits wide linewidths of tens to hundreds of nanometers, which limits the sensing performance. In plasmonic nanolaser cavity, these

dampings can be fully compensated by the gain medium, which can reduce the plasmonic resonant linewidth by two orders of magnitude. Therefore, plasmonic nanolasers have potential applications in biochemical sensing.

In the area of gas sensors, as shown in **Figure 13a**, plasmonic nanosensors have been shown to detect explosion molecules in air with a sensitivity of parts per billion under normal conditions.<sup>[40]</sup> As shown in **Figure 13b**, the sensitivities for DNT, AN and NB can be calculated by the slope of the calibration curves. The sensitivity of the stimulated emission in plasmonic nanolaser is 300-fold as greater as that of spontaneous emission.

The sensing mechanism is that gas molecules influence the rate of surface recombination through interactions with surface states. However, there is a limitation: due to the small size requirement of gain materials in plasmonic nanolaser, the material surface that be affected by gas molecules will be reduced accordingly, and its efficiency will be affected to some extent.

In the area of refractive index sensors, Lu group proposed a refractive index sensor using hollow defect plasmonic nanocavity (Figure 13c).<sup>[44]</sup> The physical mechanism is that Al grating as hybrid plasmonic Bragg reflector to enhance the light-matter coupling in the cavity and use that enhanced light field to achieve refractive index sensing. The simulation results show that the sensor has very high sensitivity and high resolution in glucose solution at the resonant wavelength of 373 nm (Figure 13d). The plasmonic nanolasers as refractive index sensor requires surface passivation step to improve its stability. A recent experiment showed that the plasmonic nanolaser sensor with a 7 nm Al<sub>2</sub>O<sub>3</sub> passivation layer did not degrade significantly within a few hours, while the nanolaser without passivation layer lasted only a few seconds.<sup>[43]</sup>

The spaser composed of the optical resonator of plasmonic NPs coated with the gain medium, has advantages of single mode emitting by a spectrally tunable laser, bright light fundamentally without optical saturation at high laser intensity, blinking effects and the spectral crosstalk between fluorophores. This supports a series of biosensing analysis, including protein molecular detection, cell labeling and tracking, and high-definition intracellular imaging.

Recently, the multiple functions of spaser have been demonstrated in complicated biological contexts, ranging from cytoplasm in vitro to mouse tissues in vivo.<sup>[45]</sup> It can be applied directly to living cells and animal tissues as an ultra-bright, water-soluble and biocompatible probe. As shown in Figure 13e, lasing performance of the spaser show a stronger emission intensity of 4100 times and narrower spectral width of 30 time, respectively, than that of quantum dots. In addition, the silica surface of spaser is functionalized with folic acid through molecular covalently binding for the targeted recognition of tumor cells (Figure 13f). Integration of these properties enables nanobubble spaser to exhibit great potential as a promising multimodal, high resolution and ultrafast cellular probe capable of achieving in vitro and intracellular biomedical assays with a single-pulse nanosecond excitation. Similarly, using ultra narrow spectral linewidth of the spaser as probes (Figure 13g), a new concept of spaser-stimulated emission depletion (STED) through collecting the stimulated emission of spaser as the imaging signal has been published recently.<sup>[46]</sup> Compare to confocal imaging of aggregate or monodispersed spaser nanoparticles, it is clear that, STED imaging is higher resolution. As shown in Figure 13h, the resolution of the spaser-STED is 3.8 times as narrower as that of confocal. In principle, the Spaser's wavelength can be adjusted in the visible region. If the "SPASER probe family" are built, they have great potential in most fluorescence-based analysis.

### 5.3. Far-Field Applications

The spaser formed by a single metal NP has only one SPR feedback, resulting in the spectra emission with low quality factor

and no directionality. The collective oscillation of metallic NPs array called surface lattice resonance (SLR) has an outstanding characteristic with the narrow linewidth of the output signal and low laser threshold. The characteristic of the SLR eigenmode engineering can be controlled by coupling, relative phase, eigenmode symmetry and topology. Different from one SPR feedback, the macroscopic laser field of SLR eigenmode engineering can achieve can realize far-field applications.

The concept of lasing arrays to achieve high quality factors was originally reported for the mid-IR split-ring resonator array. Then, the lasing spaser of various metal nanoarrays embedded in organic gain media and quantum dots has been realized in experiments. As shown in Figure 14a, 3D gold bowtie NPs array nanolaser in mid-IR wavelength can realize laser operation.<sup>[50]</sup> Due to enhanced emission cross section by the plasmonic nanocavity formed by the Au bowties. The Au bowties as SPR feedback can improve the gain and SP-assisted lasing behavior can generate at room temperature. A significant advantage of NPs array lasers is their emission wavelength tunability. Laser wavelength tunability is achieved by dynamically feeding different refractive index gain materials into Au NPs arrays. The eigenmode of the metal array is limited by the inherent design. Plasmonic superlattices, which consists of several groups of Au arrays with different periods, can support multiple band-edge modes. The multiple eigenmodes with large mode spacings superlattices are capable of multi-modal nanolasing which can realize switchable lasing between single mode and multiple modes. In addition, laser mode in plasmonic array laser is also adjusted by applying stress. Robust stretchable nanolasing in compact stretchable device consisted of a flexible PDMS substrate, large Au NP arrays supporting hybrid quadrupole lattice (HQLs) plasmons and liquid dye molecules<sup>[57]</sup> was realized in Figure 14b. The device can be adjustable wavelength through stretching and releasing the flexible PDMS substrate which the cavity resonance can be directly changed by adjusting interparticle distances.

Due to the gain limited to mixed concentration of dyes, quantum dots, above mentioned SLR plasmonic lasers require relatively large array to enhance gain feedback. In addition, the overlap between near field in metallic NPs and those gain medium is not large enough, resulting in hindering light and matter interaction. Huang et al. proposed the hybrid plasmonic SLR laser composed of a CH<sub>3</sub>NH<sub>3</sub>PbBr<sub>3</sub> thin film and Ag NPs array (Figure 14c). The relatively high gain of the CH<sub>3</sub>NH<sub>3</sub>PbBr<sub>3</sub> thin film can enhance the light-matter interaction, resulting in high  $\beta$  and low threshold lasing.<sup>[64]</sup>

## 6. Conclusion and Outlook

We review recent low-threshold plasmonic nanolasers and related applications. Although the plasmonic nanolaser satisfies the need of coherent light source miniaturization, the high power consumption of the device still has a certain impact on the practical application. According to the theoretical study, the factors that affect the threshold of the plasmonic nanolaser include cavity loss (radiation loss and metal loss), material loss and spontaneous radiation coupling factor  $\beta$ .

On the one hand, the threshold can reduce via using high gain materials and metals of low plasmon loss. The commonly used high-gain materials are: II–VI semiconductors, III–V

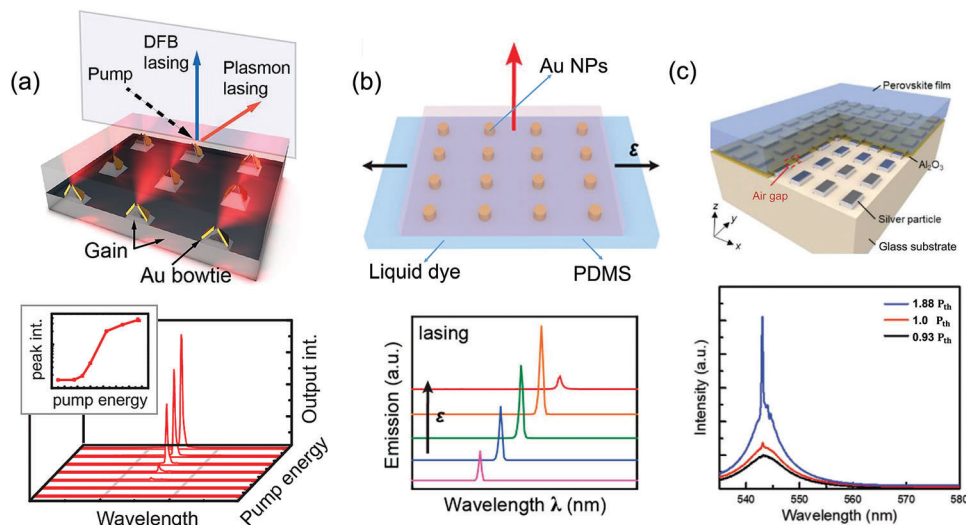


**Figure 14.** a) Upper panel: Schematic diagram of 3D bowtie plasmonic laser. Lower panel: The power-dependent photoluminescence (PL) spectra from 3D Au bowties. Reproduced with permission.<sup>[50]</sup> Copyright 2012, ACS. b) Upper panel: Stretchable SLR nanolasing. Lower panel: Schematic diagram of a wavelength tunable nanolaser with strain  $\epsilon$  applied on flexible PDMS substrate. Reproduced with permission.<sup>[57]</sup> Copyright 2018, ACS. c) Upper panel: Scheme of the hybrid plasmonic SLR MAPbBr<sub>3</sub> laser on the Ag NP array. Lower panel: Evolution of lasing spectra of hybrid plasmonic SLR MAPbBr<sub>3</sub> laser is measured. Reproduced with permission.<sup>[64]</sup> Copyright 2021, Wiley-VCH.

semiconductors, perovskite, InP, dyes and so on. Obviously, the use of high quality gain materials (include the high crystal quality and cavity quality) can reduce material loss and radiation loss in the device. For the metal aspect, besides Al (UV region), Ag (visible and infrared region), Au (visible region), the most breakthrough is the use of sodium (Na) film in the infrared region. Metal loss can be reduced by optimizing the roughness of the metal surface and introducing graphene to regulate the surface electron density of the metal.

On the other hand, strong Purcell effect caused by small cavity will enhance the interaction of light and matter, resulting in large  $\beta$  (the lasing output looks like “thresholdless”). However, the enhanced spontaneous emission and the enhanced nonradiative channels makes the difficulty of population inversion, resulting in the increase of laser threshold. The threshold can be reduced by the optimizing structure design of the optical confinement. For example, compared with the FP cavity, the whispering gallery mode (WGM) cavity can achieve a smaller radiation loss, leading to smaller cavity loss. Then, according to formula  $R_{th} = \gamma/\Gamma$ , obviously, the latter can achieve a lower threshold.

In addition, low temperature is also a means to reduce the threshold, because low temperature not only reduce the plasmon loss of metals and improve luminescence of semiconductor materials, but also increase the proportion of pump power absorbed by gain medium (For an optically-pumped nanolaser, most of absorbed power is easily converted to heat at room temperature, and only a small portion is utilized in the generation of emitted light).

According to information of plasmonic nanolaser in Section 4, we assumed that  $\tau_0 \approx 10^{-9}$  s (for organic and inorganic semiconductor gain media);  $\gamma^{-1}$  is 10 fs–100 fs;  $\beta F_p = 1 - 10$  and  $N = \Gamma n_{inv} V_{phy} \approx 10^5$ . We can estimate that  $\zeta$  is  $10^{-2} \sim 1$  for plasmonic nanolaser. In **Figure 15**, the approximate range of threshold for the three lasers is given. It is seen that threshold of plas-

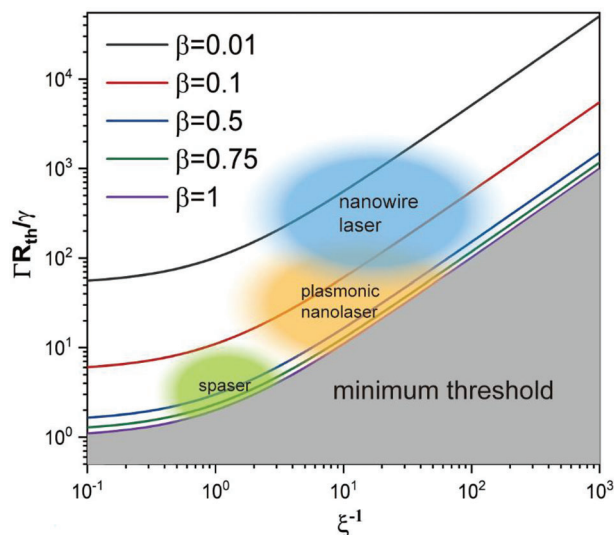


**Figure 15.** Normalized threshold as a function of the  $\zeta$  and  $\beta$  parameters with three type nanolaser.

monic nanolaser is less than nanowire laser (photonic nanolaser with small volume).<sup>[124]</sup> However,  $\zeta < 1$  for semiconductor lasers indicates that material loss is dominant. Only when  $\zeta \rightarrow 1$ , the threshold reaches its minimum value. For the spaser,  $\zeta \rightarrow 1$  is possible. And the strong confinement of the LSP allows the  $\beta$  to approach 1. As shown in **Figure 15**, these conditions allow the spaser to operate with a minimum threshold. Thanks to strong confinement and high gain, the spaser can operate at near optimal conditions for threshold energy consumption. If the difficulties and challenges brought by preparation can be overcome, the “SPASER probe family” will increase more possibilities for biochemical analysis applications.

In the aspect of electric pumped plasmons laser, the mature nanolaser fabrication technology is also essential, which can reduce cavity loss generated by roughness and the self-heat generated during the operation of devices. Combined with the far-field radiation theory, it is possible to be applied to commercial optical interconnection and integrated on-chips.

## Acknowledgements

The authors thank the support of the National Natural Science Foundation of China (No. 52125205, U20A20166, 52192614, U22A2077, and 52002246), National key R&D Program of China (2021YFB3200302 and 2021YFB3200304), Natural Science Foundation of Beijing Municipality (Z180011 and 2222088), Shenzhen Science and Technology Program (Grant No. KQTD20170810105439418), the Shenzhen Fundamental Research Project (JCYJ20190808170601664), the Science and Technology Innovation Project of Shenzhen Excellent Talents (RCBS20200714114919006), and the Fundamental Research Funds for the Central Universities.

## Conflict of Interest

The authors declare no conflict of interest.

## Keywords

low threshold, plasmonic nanolasers, semiconductor lasers, spaser, surface plasmons

Received: January 5, 2023

Revised: April 19, 2023

Published online:

- [1] T. H. Maiman, *Nature* **1960**, 187, 493.
- [2] D. Zhang, Y. Zeng, Y. Bai, Z. Li, Y. Tian, R. Li, *Nature* **2022**, 611, 55.
- [3] K. Y. Jeong, M. S. Hwang, J. Kim, J. S. Park, J. M. Lee, H. G. Park, *Adv. Mater.* **2020**, 32, 2001996.
- [4] M. Wang, F. R. Cao, L. Li, *Small Struct.* **2022**, 3, 2100165.
- [5] H. Soda, K. Iga, C. Kitahara, Y. Suematsu, *Jpn. J. Appl. Phys.* **1979**, 18, 2329.
- [6] T.-C. Chang, S.-Y. Kuo, J.-T. Lian, K.-B. Hong, S.-C. Wang, T.-C. Lu, *Appl. Phys. Express* **2017**, 10, 112101.
- [7] S. L. McCall, A. F. J. Levi, R. E. Slusher, S. J. Pearton, R. A. Logan, *Appl. Phys. Lett.* **1992**, 60, 289.
- [8] L. N. He, S. K. Ozdemir, L. Yang, *Laser Photonics Rev.* **2013**, 7, 60.
- [9] Y. Akahane, T. Asano, B. S. Song, S. Noda, *Nature* **2003**, 425, 944.
- [10] F. Raineri, A. M. Yacomotti, T. J. Karle, R. Hostein, R. Braive, A. Beveratos, I. Sagnes, R. Raj, *Opt. Express* **2009**, 17, 3165.
- [11] K. Ohashi, K. Nishi, T. Shimizu, M. Nakada, J. Fujikata, J. Ushida, S. Torii, K. Nose, M. Mizuno, H. Yukawa, M. Kinoshita, N. Suzuki, A. Gomyo, T. Ishi, D. Okamoto, K. Furue, T. Ueno, T. Tsuchizawa, T. Watanabe, K. Yamada, S. Itabashi, J. Akedo, *Proc. IEEE* **2009**, 97, 1186.
- [12] Z. P. Zhou, B. Yin, J. Michel, *Light: Sci. Appl.* **2015**, 4, 358.
- [13] K. X. Rong, F. Y. Gan, K. B. Shi, S. S. Chu, J. J. Chen, *Adv. Mater.* **2018**, 30, 1706546.
- [14] X. Z. Wei, X. G. Luo, X. C. Dong, C. L. Du, *Opt. Express* **2007**, 15, 14177.
- [15] H. B. Xie, B. Zhao, J. L. Cheng, S. K. Chamoli, T. T. Zou, W. Xin, J. J. Yang, *Nanophotonics* **2021**, 10, 3831.
- [16] J. H. Choi, Y. S. No, J. P. So, J. M. Lee, K. H. Kim, M. S. Hwang, S. H. Kwon, H. G. Park, *Nat. Commun.* **2016**, 7, 11569.
- [17] M. I. Stockman, *Science* **2015**, 348, 287.
- [18] M. I. Stockman, K. Kneipp, S. I. Bozhevolnyi, S. Saha, A. Dutta, J. Ndukaife, N. Kinsey, H. Reddy, U. Guler, V. M. Shalaev, A. Boltasseva, B. Gholipour, H. N. S. Krishnamoorthy, K. F. MacDonald, C. Soci, N. I. Zheludev, V. Savinov, R. Singh, P. Groß, C. Lienau, M. Vadai, M. L. Solomon, D. R. Barton, M. Lawrence, J. A. Dionne, S. V. Boriskina, R. Esteban, J. Aizpurua, X. Zhang, S. Yang, et al., *J. Opt.* **2018**, 20, 043001.
- [19] J. Schuller, E. S. Barnard, W. S. Cai, Y. C. Jun, J. S. White, M. L. Brongersma, *Nat. Mater.* **2010**, 9, 193.
- [20] J. Duan, J. Liu, Y. Zhang, C. Trautmann, D. Y. Lei, *J. Mater. Chem. C* **2016**, 4, 3956.
- [21] J. B. Khurgin, G. Sun, *Nanophotonics* **2012**, 1, 3.
- [22] R. X. Yan, D. Gargas, P. D. Yang, *Nat. Photonics* **2009**, 3, 569.
- [23] X. Guo, Y. B. Ying, L. M. Tong, *Acc. Chem. Res.* **2014**, 47, 656.
- [24] M. L. Brongersma, V. M. Shalaev, *Science* **2010**, 328, 440.
- [25] P. R. West, S. Ishii, G. V. Naik, N. K. Emani, V. M. Shalaev, A. Boltasseva, *Laser Photonics Rev.* **2010**, 4, 795.
- [26] A. V. Krasavin, P. Ginzburg, A. V. Zayats, *Laser Photonics Rev.* **2018**, 12, 1700082.
- [27] A. V. Zayats, I. I. Smolyaninov, A. A. Maradudin, *Phys. Rep.* **2005**, 408, 131.
- [28] D. K. Gramotnev, S. I. Bozhevolnyi, *Nat. Photonics* **2010**, 4, 83.
- [29] D. J. Bergman, M. I. Stockman, *Phys. Rev. Lett.* **2003**, 90, 027402.
- [30] M. A. Noginov, G. Zhu, A. M. Belgrave, R. Bakker, V. M. Shalaev, E. E. Narimanov, S. Stout, E. Herz, T. Suteewong, U. Wiesner, *Nature* **2009**, 460, 1110.
- [31] R. F. Oulton, V. J. Sorger, T. Zentgraf, R. M. Ma, C. Gladden, L. Dai, G. Bartal, X. Zhang, *Nature* **2009**, 461, 629.
- [32] M. T. Hill, *Opt. Express* **2009**, 17, 11107.
- [33] D. A. Genov, R. F. Oulton, G. Bartal, X. Zhang, *Phys. Rev. B* **2011**, 83, 245312.
- [34] D. Y. Fedyanin, A. V. Krasavin, A. V. Arsenin, A. V. Zayats, *Nano Lett.* **2012**, 12, 2459.
- [35] R. M. Ma, X. Yin, R. F. Oulton, V. J. Sorger, X. Zhang, *Nano Lett.* **2012**, 12, 5396.
- [36] M. K. Kim, Z. Li, K. Huang, R. Goings, M. C. Wu, H. Choo, *Opt. Express* **2013**, 21, 25796.
- [37] K. Liu, N. Li, D. K. Sadana, V. J. Sorger, *ACS Photonics* **2016**, 3, 233.
- [38] V. Dolores-Calzadilla, B. Romeira, F. Pagliano, S. Birindelli, A. Higuera-Rodriguez, P. J. van Veldhoven, M. K. Smit, A. Fiore, D. Heiss, *Nat. Commun.* **2017**, 8, 14323.
- [39] H. Li, Z. T. Huang, K. B. Hong, C. Y. Hsu, J. W. Chen, C. W. Cheng, K. P. Chen, T. R. Lin, S. J. Gwo, T. C. Lu, *Adv. Sci. (Weinh)* **2020**, 7, 2001823.
- [40] R. M. Ma, S. Ota, Y. Li, S. Yang, X. Zhang, *Nat. Nanotechnol.* **2014**, 9, 600.
- [41] A. Yang, T. B. Hoang, M. Dridi, C. Deeb, M. H. Mikkelsen, G. C. Schatz, T. W. Odom, *Nat. Commun.* **2015**, 6, 6939.
- [42] P. Melentiev, A. Kalmykov, A. Gritchenko, A. Afanasiev, V. Balykin, A. S. Baburin, E. Ryzhova, I. Filippov, I. A. Rodionov, I. A. Nechepurenko, A. V. Dorofeenko, I. Ryzhikov, A. P. Vinogradov, A. A. Zyablovsky, E. S. Andrianov, A. A. Lisyansky, *Appl. Phys. Lett.* **2017**, 111, 213104.
- [43] S. Wang, B. Li, X.-Y. Wang, H.-Z. Chen, Y.-L. Wang, X.-W. Zhang, L. Dai, R.-M. Ma, *ACS Photonics* **2017**, 4, 1355.
- [44] P.-J. Cheng, Z.-T. Huang, J.-H. Li, B.-T. Chou, Y.-H. Chou, W.-C. Lo, K.-P. Chen, T.-C. Lu, T.-R. Lin, *ACS Photonics* **2018**, 5, 2638.
- [45] E. I. Galanzha, R. Weingold, D. A. Nedosekin, M. Sarimollaoglu, J. Nolan, W. Harrington, A. S. Kuchyanov, R. G. Parkhomenko, F.

- Watanabe, Z. Nima, A. S. Biris, A. I. Plekhanov, M. I. Stockman, V. P. Zharov, *Nat. Commun.* **2017**, *8*, 15528.
- [46] Z. Gao, J. H. Wang, P. Song, B. Kang, J. J. Xu, H. Y. Chen, *Adv. Mater.* **2020**, *32*, 1907233.
- [47] J.-H. Wang, Z. Gao, P. Song, P. N. Melentiev, X.-H. Wang, H. Gao, F. Yang, B. Kang, J.-J. Xu, H.-Y. Chen, *J. Phys. Chem. C* **2020**, *124*, 16553.
- [48] N. I. Zheludev, S. L. Prosvirnin, N. Papisimakis, V. A. Fedotov, *Nat. Photonics* **2008**, *2*, 351.
- [49] S. R. K. Rodriguez, A. Abass, B. Maes, O. T. A. Janssen, G. Vecchi, J. Gómez Rivas, *Phys. Rev. X* **2011**, *1*, 021019.
- [50] J. Y. Suh, C. H. Kim, W. Zhou, M. D. Huntington, D. T. Co, M. R. Wasielewski, T. W. Odom, *Nano Lett.* **2012**, *12*, 5769.
- [51] W. Zhou, M. Dridi, J. Y. Suh, C. H. Kim, D. T. Co, M. R. Wasielewski, G. C. Schatz, T. W. Odom, *Nat. Nanotechnol.* **2013**, *8*, 506.
- [52] A. K. Yang, Z. Y. Li, M. P. Knudson, A. J. Hryn, W. J. Wang, K. Aydin, T. W. Odom, *ACS Nano* **2015**, *9*, 11582.
- [53] C. Zhang, Y. Lu, Y. Ni, M. Li, L. Mao, C. Liu, D. Zhang, H. Ming, P. Wang, *Nano Lett.* **2015**, *15*, 1382.
- [54] T. K. Hakala, H. T. Rekola, A. I. Vakevainen, J. P. Martikainen, M. Necada, A. J. Moilanen, P. Torma, *Nat. Commun.* **2017**, *8*, 13687.
- [55] T. B. Hoang, G. M. Akselrod, A. Yang, T. W. Odom, M. H. Mikkelsen, *Nano Lett.* **2017**, *17*, 6690.
- [56] D. Wang, A. Yang, W. Wang, Y. Hua, R. D. Schaller, G. C. Schatz, T. W. Odom, *Nat. Nanotechnol.* **2017**, *12*, 889.
- [57] D. Wang, M. R. Bourgeois, W. K. Lee, R. Li, D. Trivedi, M. P. Knudson, W. Wang, G. C. Schatz, T. W. Odom, *Nano Lett.* **2018**, *18*, 4549.
- [58] A. Fernandez-Bravo, D. Wang, E. S. Barnard, A. Teitelboim, C. Tajon, J. Guan, G. C. Schatz, B. E. Cohen, E. M. Chan, P. J. Schuck, T. W. Odom, *Nat. Mater.* **2019**, *18*, 1172.
- [59] S. Pourjamal, T. K. Hakala, M. Necada, F. Freire-Fernandez, M. Kataja, H. Rekola, J. P. Martikainen, P. Torma, S. van Dijken, *ACS Nano* **2019**, *13*, 5686.
- [60] Y. H. Hsieh, B. W. Hsu, K. N. Peng, K. W. Lee, C. W. Chu, S. W. Chang, H. W. Lin, T. J. Yen, Y. J. Lu, *ACS Nano* **2020**, *14*, 11670.
- [61] J. M. Taskinen, A. J. Moilanen, H. Rekola, K. Kuntze, A. Priimagi, P. Törmä, T. K. Hakala, *ACS Photonics* **2020**, *7*, 2850.
- [62] D. Wang, M. R. Bourgeois, J. Guan, A. K. Fumani, G. C. Schatz, T. W. Odom, *ACS Photonics* **2020**, *7*, 630.
- [63] J. M. Winkler, M. J. Ruckriegel, H. Rojo, R. C. Keitel, E. De Leo, F. T. Rabouw, D. J. Norris, *ACS Nano* **2020**, *14*, 5223.
- [64] Z. T. Huang, C. W. Yin, Y. H. Hong, H. Li, K. B. Hong, T. S. Kao, M. H. Shih, T. C. Lu, *Adv. Opt. Mater.* **2021**, *9*, 2100299.
- [65] Y. G. Sang, J. Y. Lu, Y. H. Ouyang, H. Y. Luan, J. H. Wu, J. Y. Li, R. M. Ma, *Nat. Commun.* **2022**, *13*, 6485.
- [66] W. L. Barnes, A. Dereux, T. W. Ebbesen, *Nature* **2003**, *424*, 824.
- [67] M. C. Daniel, D. Astruc, *Chem. Rev.* **2004**, *104*, 293.
- [68] S. Y. Ding, J. Yi, J. F. Li, B. Ren, D. Y. Wu, R. Panneerselvam, Z. Q. Tian, *Nat. Rev. Mater.* **2016**, *1*, 16021.
- [69] V. G. Kravets, A. V. Kabashin, W. L. Barnes, A. N. Grigorenko, *Chem. Rev.* **2018**, *118*, 5912.
- [70] G. Eda, S. A. Maier, *ACS Nano* **2013**, *7*, 5660.
- [71] X. Han, Z. S. Xu, W. Q. Wu, X. H. Liu, P. G. Yan, C. F. Pan, *Small Struct.* **2020**, *1*, 2000029.
- [72] S. Z. Wang, A. A. Y. Amin, L. Z. Wu, M. H. Cao, Q. Zhang, T. Ameri, *Small Struct.* **2021**, *2*, 2000124.
- [73] E. Boisselier, D. Astruc, *Chem. Soc. Rev.* **2009**, *38*, 1759.
- [74] J. N. Anker, W. P. Hall, O. Lyandres, N. C. Shah, J. Zhao, R. P. Van Duyne, *Nat. Mater.* **2008**, *7*, 442.
- [75] K. Saha, S. S. Agasti, C. Kim, X. N. Li, V. M. Rotello, *Chem. Rev.* **2012**, *112*, 2739.
- [76] X. Liu, F. Zhang, R. Huang, C. Pan, J. Zhu, *Cryst. Growth Des.* **2008**, *8*, 1916.
- [77] M. Ibrar, S. E. Skrabalak, *Small Struct.* **2021**, *2*, 2100043.
- [78] S. A. Maier, H. A. Atwater, *J. Appl. Phys.* **2005**, *98*, 011101.
- [79] K. C. Vernon, A. M. Funston, C. Novo, D. E. Gomez, P. Mulvaney, T. J. Davis, *Nano Lett.* **2010**, *10*, 2080.
- [80] G. C. Li, Y. L. Zhang, J. Jiang, Y. Luo, D. Y. Lei, *ACS Nano* **2017**, *11*, 3067.
- [81] D. B. Li, X. J. Sun, Y. P. Jia, M. I. Stockman, H. P. Paudel, H. Song, H. Jiang, Z. M. Li, *Light: Sci. Appl.* **2017**, *6*, e17038.
- [82] Y. Wang, C. Xu, J. Li, J. Dai, Y. Lin, G. Zhu, J. Lu, *Sci. Adv. Mater.* **2015**, *7*, 1156.
- [83] J. Lu, C. Xu, J. Dai, J. Li, Y. Wang, Y. Lin, P. Li, *Nanoscale* **2015**, *7*, 3396.
- [84] J. T. Li, Y. Lin, J. F. Lu, C. X. Xu, Y. Y. Wang, Z. L. Shi, J. Dai, *ACS Nano* **2015**, *9*, 6794.
- [85] J. Li, M. Jiang, C. Xu, Y. Wang, Y. Lin, J. Lu, *Sci. Rep.* **2015**, *5*, 9263.
- [86] J. Lu, C. Xu, J. Dai, J. Li, Y. Wang, Y. Lin, P. Li, *ACS Photonics* **2014**, *2*, 73.
- [87] C. Huang, C. Xu, J. Lu, Z. Li, Z. Tian, *Appl. Surf. Sci.* **2016**, *365*, 291.
- [88] J. Lu, Z. Shi, Y. Wang, Y. Lin, Q. Zhu, Z. Tian, J. Dai, S. Wang, C. Xu, *Sci. Rep.* **2016**, *6*, 25645.
- [89] J. Lu, C. Xu, H. Nan, Q. Zhu, F. Qin, A. G. Manohari, M. Wei, Z. Zhu, Z. Shi, Z. Ni, *Appl. Phys. Lett.* **2016**, *109*, 073701.
- [90] J. Lu, C. Xu, Z. Tian, J. Lu, Y. Lin, Z. Shi, *Nanoscale* **2016**, *8*, 5120.
- [91] J. Lu, Q. Zhu, Z. Zhu, Y. Liu, M. Wei, Z. Shi, C. Xu, *J. Mater. Chem. C* **2016**, *4*, 7718.
- [92] Y. Y. Wang, C. X. Xu, M. M. Jiang, J. T. Li, J. Dai, J. F. Lu, P. L. Li, *Nanoscale* **2016**, *8*, 16631.
- [93] Q. Zhu, J. Lu, Y. Wang, F. Qin, Z. Shi, C. Xu, *Sci. Rep.* **2016**, *6*, 36194.
- [94] F. Qin, N. Chang, C. Xu, Q. Zhu, M. Wei, Z. Zhu, F. Chen, J. Lu, *RSC Adv.* **2017**, *7*, 15071.
- [95] Y. Wang, F. Qin, J. Lu, J. Li, Z. Zhu, Q. Zhu, Y. Zhu, Z. Shi, C. Xu, *Nano Res.* **2017**, *10*, 3447.
- [96] Y. Z. Zhu, H. Guo, Q. N. Cui, J. P. Chen, Z. X. Li, J. F. Lu, T. C. Lu, Z. C. Peng, C. X. Xu, C. F. Pan, *Laser Photonics Rev.* **2023**, *17*, 2200497.
- [97] Q. Zhu, F. Qin, J. Lu, Z. Zhu, H. Nan, Z. Shi, Z. Ni, C. Xu, *Nano Res.* **2017**, *10*, 1996.
- [98] F. Qin, C. Xu, D. Y. Lei, S. Li, J. Liu, Q. Zhu, Q. Cui, D. You, A. G. Manohari, Z. Zhu, F. Chen, *ACS Photonics* **2018**, *5*, 2313.
- [99] F. F. Qin, C. X. Xu, Q. X. Zhu, J. F. Lu, D. T. You, W. Xu, Z. Zhu, A. G. Manohari, F. Chen, *Nanoscale* **2018**, *10*, 623.
- [100] X. X. Wang, C. X. Xu, F. F. Qin, Y. J. Liu, A. G. Manohari, D. T. You, W. Liu, F. Chen, Z. L. Shi, Q. N. Cui, *Nanoscale* **2018**, *10*, 17852.
- [101] C. Xu, F. Qin, Q. Zhu, J. Lu, Y. Wang, J. Li, Y. Lin, Q. Cui, Z. Shi, A. G. Manohari, *Nano Res.* **2018**, *11*, 3050.
- [102] Q. Zhu, C. Xu, D. Wang, B. Liu, F. Qin, Z. Zhu, Y. Liu, X. Zhao, Z. Shi, *J. Mater. Chem. C* **2019**, *7*, 2710.
- [103] J. A. Dionne, L. A. Sweatlock, H. A. Atwater, A. Polman, *Phys. Rev. B* **2005**, *72*, 075405.
- [104] P. Berini, I. De Leon, *Nat. Photonics* **2012**, *6*, 16.
- [105] K. Li, X. Li, M. I. Stockman, D. J. Bergman, *Phys. Rev. B* **2005**, *71*, 115409.
- [106] M. I. Stockman, *J. Opt.* **2010**, *12*, 024004.
- [107] D. Li, M. I. Stockman, *Phys. Rev. Lett.* **2013**, *110*, 106803.
- [108] R. F. Oulton, V. J. Sorger, D. A. Genov, D. F. P. Pile, X. Zhang, *Nat. Photonics* **2008**, *2*, 496.
- [109] J. B. Khurgin, M. A. Noginov, *Laser Photonics Rev.* **2021**, *15*, 2000250.
- [110] M. P. Nezhad, A. Simic, O. Bondarenko, B. Slutsky, A. Mizrahi, L. Feng, V. Lomakin, Y. Fainman, *Nat. Photonics* **2010**, *4*, 395.
- [111] S. W. Chang, T. R. Lin, S. L. Chuang, *Opt. Express* **2010**, *18*, 15039.
- [112] R.-M. Ma, R. F. Oulton, V. J. Sorger, X. Zhang, *Laser Photonics Rev.* **2013**, *7*, 1.
- [113] L. W. Casperson, *J. Appl. Phys.* **1975**, *46*, 5194.
- [114] R. M. Ma, R. F. Oulton, *Nat. Nanotechnol.* **2019**, *14*, 12.
- [115] S.-L. Wang, S. Wang, X.-K. Man, R.-M. Ma, *Nanophotonics* **2020**, *9*, 3403.
- [116] R. Roder, T. P. Sidiropoulos, C. Tessarek, S. Christiansen, R. F. Oulton, C. Ronning, *Nano Lett.* **2015**, *15*, 4637.

- [117] V. J. Sorger, N. Pholchai, E. Cubukcu, R. F. Oulton, P. Kolchin, C. Borschel, M. Gnauck, C. Ronning, X. Zhang, *Nano Lett.* **2011**, *11*, 4907.
- [118] Y.-H. Chou, K.-B. Hong, Y.-C. Chung, C.-T. Chang, B.-T. Chou, T.-R. Lin, S. M. Arakelian, A. P. Alodjants, T.-C. Lu, *IEEE J. Sel. Top. Quantum Electron.* **2017**, *23*, 4601907.
- [119] Y. C. Chung, P. J. Cheng, Y. H. Chou, B. T. Chou, K. B. Hong, J. H. Shih, S. D. Lin, T. C. Lu, T. R. Lin, *Sci. Rep.* **2017**, *7*, 39813.
- [120] J. Lu, M. Jiang, M. Wei, C. Xu, S. Wang, Z. Zhu, F. Qin, Z. Shi, C. Pan, *ACS Photonics* **2017**, *4*, 2419.
- [121] H. Yu, T. P. H. Sidiropoulos, W. Liu, C. Ronning, P. K. Petrov, S.-H. Oh, S. A. Maier, P. Jin, R. F. Oulton, *Adv. Opt. Mater.* **2017**, *5*, 1600856.
- [122] C. Y. Wu, C. T. Kuo, C. Y. Wang, C. L. He, M. H. Lin, H. Ahn, S. Gwo, *Nano Lett.* **2011**, *11*, 4256.
- [123] T. Tao, T. Zhi, B. Liu, J. Dai, Z. Zhuang, Z. Xie, P. Chen, F. Ren, D. Chen, Y. Zheng, R. Zhang, *Adv. Funct. Mater.* **2017**, *27*, 1703198.
- [124] S. Wang, X. Y. Wang, B. Li, H. Z. Chen, Y. L. Wang, L. Dai, R. F. Oulton, R. M. Ma, *Nat. Commun.* **2017**, *8*, 1889.
- [125] H.-Z. Chen, S. Wang, R.-M. Ma, *IEEE J. Quantum Electron.* **2018**, *54*, 7200307.
- [126] Z. Wu, J. Chen, Y. Mi, X. Sui, S. Zhang, W. Du, R. Wang, J. Shi, X. Wu, X. Qiu, Z. Qin, Q. Zhang, X. Liu, *Adv. Opt. Mater.* **2018**, *6*, 1800674.
- [127] Y.-J. Lu, T. L. Shen, K.-N. Peng, P.-J. Cheng, S.-W. Chang, M.-Y. Lu, C. W. Chu, T.-F. Guo, H. A. Atwater, *ACS Photonics* **2020**, *8*, 335.
- [128] J. Wang, X. Jia, Z. Wang, W. Liu, X. Zhu, Z. Huang, H. Yu, Q. Yang, Y. Sun, Z. Wang, S. Qu, J. Lin, P. Jin, Z. Wang, *Nanoscale* **2020**, *12*, 16403.
- [129] J. Wang, X. Jia, Y. Guan, K. Ren, H. Yu, Z. Wang, S. Qu, Q. Yang, J. Lin, Z. Wang, P. Jin, *Laser Photonics Rev.* **2021**, *15*, 2000512.
- [130] X. Jia, J. Wang, Z. Huang, K. Chu, K. Ren, M. Sun, Z. Wang, P. Jin, K. Liu, S. Qu, *J. Mater. Chem. C* **2022**, *10*, 680.
- [131] S.-H. Kwon, J.-H. Kang, S.-K. Kim, H.-G. Park, *IEEE J. Quantum Electron.* **2011**, *47*, 1346.
- [132] R. Wang, C. X. Xu, D. T. You, X. X. Wang, J. P. Chen, Z. L. Shi, Q. N. Cui, T. Qiu, *Nanoscale* **2021**, *13*, 6780.
- [133] R. Wang, C. X. Xu, D. T. You, X. X. Wang, J. P. Chen, Z. L. Shi, Q. N. Cui, T. Qiu, *J. Lumin.* **2021**, *238*, 118242.
- [134] T. P. H. Sidiropoulos, R. Röder, S. Geburt, O. Hess, S. A. Maier, C. Ronning, R. F. Oulton, *Nat. Phys.* **2014**, *10*, 870.
- [135] Q. Zhang, G. Li, X. Liu, F. Qian, Y. Li, T. C. Sum, C. M. Lieber, Q. Xiong, *Nat. Commun.* **2014**, *5*, 4953.
- [136] Y. H. Chou, B. T. Chou, C. K. Chiang, Y. Y. Lai, C. T. Yang, H. Li, T. R. Lin, C. C. Lin, H. C. Kuo, S. C. Wang, T. C. Lu, *ACS Nano* **2015**, *9*, 3978.
- [137] Y. H. Chou, K. B. Hong, C. T. Chang, T. C. Chang, Z. T. Huang, P. J. Cheng, J. H. Yang, M. H. Lin, T. R. Lin, K. P. Chen, S. Gwo, T. C. Lu, *Nano Lett.* **2018**, *18*, 747.
- [138] Y. H. Chou, Y. M. Wu, K. B. Hong, B. T. Chou, J. H. Shih, Y. C. Chung, P. Y. Chen, T. R. Lin, C. C. Lin, S. D. Lin, T. C. Lu, *Nano Lett.* **2016**, *16*, 3179.
- [139] H. Li, J. H. Li, K. B. Hong, M. W. Yu, Y. C. Chung, C. Y. Hsu, J. H. Yang, C. W. Cheng, Z. T. Huang, K. P. Chen, T. R. Lin, S. Gwo, T. C. Lu, *Nano Lett.* **2019**, *19*, 5017.
- [140] R. M. Ma, R. F. Oulton, V. J. Sorger, G. Bartal, X. Zhang, *Nat. Mater.* **2011**, *10*, 110.
- [141] S. Wang, H. Z. Chen, R. M. Ma, *Nano Lett.* **2018**, *18*, 7942.
- [142] Q. Zhang, Q. Shang, J. Shi, J. Chen, R. Wang, Y. Mi, W. Du, C. Shen, R. Ma, X. Qiu, X. Liu, T. C. Sum, *ACS Photonics* **2017**, *4*, 2789.
- [143] Y. J. Lu, C. Y. Wang, J. Kim, H. Y. Chen, M. Y. Lu, Y. C. Chen, W. H. Chang, L. J. Chen, M. I. Stockman, C. K. Shih, S. Gwo, *Nano Lett.* **2014**, *14*, 4381.
- [144] Y. Z. Zhu, Q. N. Cui, J. P. Chen, F. Chen, Z. L. Shi, X. W. Zhao, C. X. Xu, *ACS Appl. Mater. Interfaces* **2021**, *13*, 6820.
- [145] K. Xia, W. Wu, M. Zhu, X. Shen, Z. Yin, H. Wang, S. Li, M. Zhang, H. Wang, H. Lu, A. Pan, C. Pan, Y. Zhang, *Sci. Bull.* **2020**, *65*, 343.
- [146] F. Li, J. Lu, Q. Zhang, D. Peng, Z. Yang, Q. Xu, C. Pan, A. Pan, T. Li, R. Wang, *Sci. Bull.* **2019**, *64*, 698.
- [147] H. Yu, K. Ren, Q. Wu, J. Wang, J. Lin, Z. Wang, J. Xu, R. F. Oulton, S. Qu, P. Jin, *Nanoscale* **2016**, *8*, 19536.
- [148] K. Ren, J. Wang, S. Chen, Q. Yang, J. Tian, H. Yu, M. Sun, X. Zhu, S. Yue, Y. Sun, K. Liu, M. Azam, Z. Wang, P. Jin, S. Qu, Z. Wang, *Laser Photonics Rev.* **2019**, *13*, 1800306.
- [149] Z. T. Huang, J. W. Chen, H. Li, Y. Zhu, Q. Cui, C. Xu, T. C. Lu, *Adv. Opt. Mater.* **2022**, *10*, 2200603.
- [150] S. H. Kwon, J. H. Kang, C. Seassal, S. K. Kim, P. Regreny, Y. H. Lee, C. M. Lieber, H. G. Park, *Nano Lett.* **2010**, *10*, 3679.
- [151] Y. Wang, J. Yu, Y. F. Mao, J. Chen, S. Wang, H. Z. Chen, Y. Zhang, S. Y. Wang, X. Chen, T. Li, L. Zhou, R. M. Ma, S. Zhu, W. Cai, J. Zhu, *Nature* **2020**, *581*, 401.
- [152] M. T. Hill, Y.-S. Oei, B. Smalbrugge, Y. Zhu, T. de Vries, P. J. van Veldhoven, F. W. M. van Otten, T. J. Eijkemans, J. P. Turkiewicz, H. de Waardt, E. J. Geluk, S.-H. Kwon, Y.-H. Lee, R. Nötzel, M. K. Smit, *Nat. Photonics* **2007**, *1*, 589.
- [153] K. Ding, Z. Liu, L. Yin, H. Wang, R. Liu, M. T. Hill, M. J. H. Marell, P. J. van Veldhoven, R. Nötzel, C. Z. Ning, *Appl. Phys. Lett.* **2011**, *98*, 041110.
- [154] K. Ding, C. Z. Ning, *Light: Sci. Appl.* **2012**, *1*, e20.
- [155] K. Ding, Z. C. Liu, L. J. Yin, M. T. Hill, M. J. H. Marell, P. J. van Veldhoven, R. Nötzel, C. Z. Ning, *Phys. Rev. B* **2012**, *85*, 041301.
- [156] S. H. Pan, Q. Gu, A. El Amili, F. Vallini, Y. Fainman, *Optica* **2016**, *3*, 1260.
- [157] S. S. Deka, S. H. Pan, S. Jiang, A. El Amili, F. Vallini, Q. Gu, Y. Fainman, *Opt. Express* **2020**, *28*, 27346.
- [158] Q. Gu, J. S. T. Smalley, J. Shane, O. Bondarenko, Y. Fainman, *Nanophotonics* **2015**, *4*, 26.
- [159] X. Yang, P. N. Ni, P. T. Jing, L. G. Zhang, R. M. Ma, C. X. Shan, D. Z. Shen, P. Genevet, *Adv. Opt. Mater.* **2019**, *7*, 1801681.
- [160] C. H. Chou, F. C. Chen, *Nanoscale* **2014**, *6*, 8444.



**Ru Wang** is currently a postdoctoral fellow in the College of Physics and Optoelectronic Engineering at Shenzhen University, China. She received a Ph.D. degree from the School of Physics, Southeast University in China in 2020. Her current research interests include plasmonic lasers and nanophotonics.



**Chunfeng Wang** received his B.S. degree in materials science and engineering from Zhengzhou University in 2013 and his Ph.D. degree in materials processing engineering from Zhengzhou University in 2019. He is currently an assistant professor in the College of Materials Science and Engineering, Shenzhen University. His research interests include optoelectronic materials and soft devices.



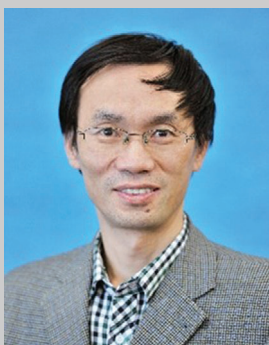
**Yi Ma** is currently a Ph.D. candidate in biological science and medical engineering at Southeast University. He received his master's degree from the Institute of Photonics, School of Physical Sciences and Technology, Ningbo University in 2020. His current research interests focus on the optical and electrical properties of wide-bandgap semiconductors.



**Jianli Sun** is a Ph.D. candidate in the School of Chemistry and Chemical Engineering at Southeast University, China, under the supervision of Prof. Chunxiang Xu. She received her B.S. in chemical engineering from the University of Jinan in 2017. Her current research focuses on microcavity laser and surface enhanced Raman scattering biosensing.



**Peiguang Yan** received his Ph.D. degree from the College of Physics Science at Nankai University, China, in 2005. He joined Shenzhen University, China, in 2005 as a lecturer, became an associate professor (2007–2012), and was then promoted to professor in 2013. His research interests include fiber optics, advanced optical fiber components, and ultrafast fiber lasers.



**Chunxiang Xu** obtained his Ph.D. degree in condensed-matter physics from the Changchun Institute of Physics, Chinese Academy of Sciences in 1997. Then he joined the School of Electronic Engineering and the School of Biological Science and Medical Engineering at Southeast University. He worked as a research fellow at Nanyang Technological University from 2003 to 2005. His current research interests focus on optoelectronic functional nanomaterials and devices.



**Caofeng Pan** received his B.S. degree (2005) and his Ph.D. (2010) in Materials Science and Engineering from Tsinghua University, China. He then joined the Georgia Institute of Technology as a post-doctoral fellow. He is currently a professor and a group leader at the Beijing Institute of Nanoenergy and Nanosystems, Chinese Academy of Sciences since 2013. His main research interests focus on the fields of low dimensional materials for fabricating smart electronic and optoelectronic devices for tactile sensing.